

Dynamics of the Equatorial Boundary Layer: A comparison of equatorial wave theory and observations

Ilana Schiller-Weiss

Master's Thesis, July 2020

Supervisor: Dr. Leo Maas



Abstract

The equatorial region ($\pm 2^\circ$ in latitude) differs from the mid-latitude regions in that there is the presence of strong zonal jets, known as equatorial deep jets. The overarching goal of this thesis is to search for eastward propagating waves that may either be explained by or produce these strong zonal currents. Equatorial zonal jets are traditionally thought to be driven by east to west surface winds, which create a pressure gradient between the eastern and western boundaries resulting in these underlying currents. As equatorial jets are stacked, with a westward, very shallow surface current and eastward undercurrent at about a 100m depth, it is ambiguous as to whether these zonal mean flows lead to instabilities in the form of waves or vice versa, whether the waves actually play a role in driving these currents. The first part of the thesis reviews the theoretical models used to describe equatorial wave theory: the linear approach assuming the beta plane approximation versus the non-traditional approach, which includes the full Coriolis term. Phase speeds for different types of waves are obtained from the dispersion relation using the two approaches.

The second part analyzes satellite sea surface height anomaly data to obtain phase speeds of propagating equatorial ocean waves and uses a spectral analysis to obtain information on spectral peaks. A 2D Fourier transform is applied to create a filter where only eastward/westward propagating signals are isolated. The focus is on eastward propagation as the Equatorial Under Current may steer waves eastward. Alternatively eastward moving waves may be rectified and drive this eastward propagating jet. By gaining insight into the properties and types of eastward moving waves, the mechanisms driving the eastward zonal jets may be more tangible, as most of the observed equatorial waves appear to propagate zonally. The Fourier filter is followed by a Radon transform to precisely determine observational phase speeds, which are then compared to theoretical phase speeds to identify different wave types. Pacific ocean wave speeds were higher on average for all frequency bands in comparison to the Atlantic and Indian oceans. When the annual cycle was removed, the presence of a mode 1 classical Rossby wave, lacking meridional nodal lines, was found in the Indian ocean. Equatorial Kelvin waves were found in the Pacific ocean at the tri-annual and 70 day cycle. A gravity and westward propagating mixed Rossby-gravity wave were found only at the 25 - 40 day period band in the Atlantic. The presence of eastward propagating Rossby waves was not confirmed from the observational data sets, however examples of classical waves were obtained.

Contents

1	General Introduction	4
2	Theory	6
2.1	Traditional, β -plane approximation	6
2.1.1	Shallow water model	7
2.1.2	Reduced gravity model (1.5 layer model)	7
2.1.3	Kelvin waves	11
2.1.4	Rosby waves	12
2.1.5	Gravity waves	13
2.1.6	Mixed Rossby-gravity waves	13
2.2	Coriolis Force	14
2.3	Nontraditional approximation	16
2.3.1	Presence of eastward Rossby waves	20
3	Observational data and pre-processing	24
3.1	Sea level anomaly data	24
3.2	Pre-processing	25
4	Results	26
4.1	Spectral analysis	26
4.2	2D Fourier Transform and Phase speeds	28
4.3	Classical Rossby waves	28
4.4	Classical Kelvin waves	33
4.5	Classical Gravity waves	37
4.6	Classical Mixed Rossby-gravity waves	40
4.7	Comparison Between LADCP Measurements taken at the Equatorial Atlantic	44
5	Discussion and Conclusions	46
5.1	Limitations and future work	47
6	Appendices	48
6.1	Appendix A: Spectral analysis: One-dimensional discrete Fourier transform	48
6.2	Appendix B: Two-dimensional Fourier transform	50
6.3	Appendix C: Radon transform	51
6.3.1	Projection-slice theorem	53
	References	56

1 General Introduction

The equatorial ocean is typically defined as reaching the extent of 2°N and 2°S in latitude. The equatorial line acts as a midpoint between the North and South poles, dividing the earth into two hemispheres. Mid and high-latitudes ocean dynamics that incorporate effects of stratification and rotation have been well-investigated, as the governing momentum equations represent mid-latitude dynamics reasonably well [1], [2]. However the effect of earth's rotation differs for the equatorial region as the latitudinal extent is very close to 0° , this is where geostrophy breaks down thus changing the role of stratification and mixing; observational evidence shows strong mixing patches in abyssal, equatorial regions from current profile measurements [3].

The longitudinal extent of the equatorial region is much greater than its latitudinal extent. The Indian and Atlantic ocean extent is reasonably comparable to one another, ≈ 6000 km in length, but the Pacific is almost four times as long. Solar insolation is concentrated at the equator, where twice a year (spring and autumn equinoxes), the sun passes directly over the equatorial line. Thus the equatorial region plays a crucial role in heat transport and exchange of ocean water between the two hemispheres [1]. Observational evidence has shown that the equatorial region, crudely speaking of $\pm 2^\circ$ or about 450 km in latitudinal extent is markedly different from higher latitudes [1], [4], [5].

The first difference between the equations governing mid-latitude and equatorial dynamics is in the use of the traditional or non-traditional treatment of the Coriolis forces. Along the equator, the latitude $\phi \approx 0^\circ$ implies that the conventional Coriolis parameter $f = 2\Omega \sin \phi$ goes to zero, where Ω is the angular velocity of the earth, which is approximated by $f \approx \beta y = 2\Omega y/a$, a denoting the earth's radius. When looking closer at the equations of motion and unpacking the Coriolis force, the parameter f is not the only one that appears in the equations [1]. The horizontal component of the Coriolis force $\tilde{f} = 2\Omega \cos \phi$ bears significance in the representation of the equations of motion, giving way to the non-traditional approach where the horizontal component is maintained. Section 2 of this master's thesis reviews the theoretical differences between the traditional, β -plane approximation with the non-traditional approach which includes the complete Coriolis force.

The second difference between higher latitudes and the equatorial zone is the presence of strong zonal currents seen from observational data on deep velocity profiles [1], [2]. A series of alternating zonal currents, or equatorial deep jets (EDJs), is present throughout the latitudinal region within $\approx \pm 2^\circ$ throughout the first hundred and even 700 meters in depth from the sea surface [1]. These strong zonal jets are peculiar yet defining features of the equatorial ocean, and the direct reasons for the presence of these EDJs still remain elusive.

Figure 1 shows the clear presence of equatorial deep jets extending a few hundred meters in the vertical at the Ceará basin, a nearly zonal channel in the Western equatorial Atlantic ocean, slightly west off the Mid-Atlantic ridge. The Ceará basin is also a conduit for northward-flowing antarctic bottom waters [1]. The thin westward current extending a few meters in depth is not present in these observations but has been observed in the equatorial Atlantic [6]. The Equatorial Under Current (EUC) is moving strongly eastward at around 110 meter depth, and there is a strong westward Equatorial Intermediate Current (EIC) around 700 m in depth. The EUC is typically attributed to westward (east to west) winds that create a build up of water on the ocean's westward shore, which creates a west to east pressure gradient driving the EUC. This idea breaks down when considering the Pacific ocean, which has a length almost four times the extent of the Indian and Atlantic ocean, where one may expect such a mechanism to show an eastward decrease in the EUC strength. However, there is actually an observed strengthening towards the eastern Pacific ocean [7], which suggests that an alternate mechanism may be driving the eastward zonal undercurrents, a mechanism that operates invariably at any zonal location.

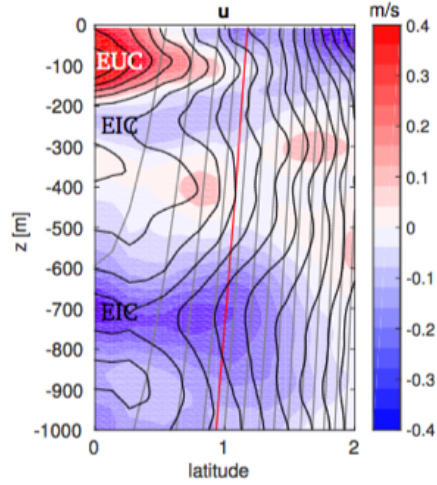


Figure 1: Zonal equatorial deep jets in the Ceará basin (LADCP velocity data image borrowed from Rabiti 2016 [1])

These stark differences between the mid-latitudes and the equatorial region can be the basis for defining the "equatorial boundary layer." The equatorial belt is interpreted as a wave guide. The presence of a pronounced thermocline and the shifting sign of the Coriolis parameter make the equatorial region a guide for different types of waves such as equatorial Kelvin, Rossby, and mixed Rossby-gravity (Yanai) waves [1], [8]. Moreover, if the earth is pictured to possess a cylindrical surface, tangent to a global ocean's floor and parallel to earth's rotation axis, the height of the homogenous density water column will decrease, vanishing completely at the equatorial surface [1]. The height is measured between ocean surfaces in the southern and northern hemispheres, and the surface along the direction parallel to the rotation axis. It is the opposite for higher latitude regions, where the height of the water column, between the ocean bottom and rigid surface, will increase with distance from the rotation axis. This will be further discussed in section 2, but the changing height of the water column is another indication for the differences between mid-latitudes and the equatorial region. It also implies that non-traditional planetary and topographic Rossby waves may be present solely within the equatorial boundary layer, further separating the equatorial region from higher latitudes.

This thesis aims to first highlight the differences in the equations of motion and dispersion relations when including the horizontal Coriolis component versus the traditional β -plane approximation. From the dispersion relations, typical wave speeds within the depth of the mixed layer are computed with the traditional approximation and then compared with non-traditional wave speeds (section 2). The goal for this is to see how the inclusion of the horizontal Coriolis component may change the dispersion curves and thus differ from the traditional phase speed estimates. Satellite altimetry data for Sea Surface Height Anomalies (SSHA) is then used to investigate the presence of an eastward propagating Rossby wave, which may be present from a theoretical standpoint but which has not yet been detected unequivocally from observational data.

Then SSHA data is looked at for all three ocean regions: equatorial Atlantic, Indian, and Pacific. A spectral analysis by use of the one-dimensional discrete Fourier transform is applied to the satellite data after preprocessing the necessary data, such as detrending and tapering. This is done to determine the dominant frequencies in the power spectrum (see appendix A). The sea level anomaly

data is then presented through longitude-time diagrams, also known as Hovmoller plots, where wave propagation can easily be seen.

The use of bandpass filters to filter/isolate certain frequencies of importance determined from the 1D spectral analysis is applied to the Hovmoller diagrams (see appendix A for more information). A 2-dimensional Fourier transform is also applied enabling another filter to isolate eastward and westward-only signals (appendix B). This allows the isolation of eastward or westward wave signals and thus makes it easier to determine different wave types from others, for example, Kelvin waves are known to propagate eastward only. A Radon transform is applied to the filtered SSHAs and then the variance is found, which enables us to determine the exact speed of the eastward or westward moving wave. The phase speeds can then be compared to the speeds found from both traditional and non-traditional equatorial wave theory, which enables the comparison between theory and observation.

The aims of this thesis can be summed up as:

1. Compute interfacial wave speeds from the traditional β -plane approximation and compare with phase speeds determined from the non-traditional, full Coriolis force approach.
2. Use observational, satellite sea level anomalies, filtered for eastward and westward signals and compute phase speeds using the Radon transform.
3. Compare the phase speeds from the observational satellite data to the theoretical ones and see if different wave types can be determined.
4. Find the presence of an eastward propagating Rossby wave by comparing the theoretical, non-traditional Rossby wave speed with the observational one.

2 Theory

2.1 Traditional, β -plane approximation

The β -plane approximation can be made for the equatorial region where the latitude reduces to 0° . In this approximation, the Coriolis parameter is taken to be the product of a constant (β) and the distance from the equator (y) [11]:

$$f = 2\Omega \sin \phi + \beta y \approx \beta y = \frac{2\Omega y}{a} \quad (1)$$

where Ω is the angular velocity of the earth 7.292124×10^{-5} rad/s, β is 2.3×10^{-11} $\text{m}^{-1}\text{s}^{-1}$, and a is the radius of the earth 6,371 km.

There are some clashes with modelling equatorial waves as linear and assuming small amplitude waves due the presence of the EDJs as seen from observational data. A linearized description of the waves is based on two specifications: one being that wave propagation is external and occurs in a barotropic fluid where the density of the fluid is solely pressure-dependent. The second description is that wave propagation is internal, meaning that the fluid is stratified (density is depth dependent) and/or rotating. In either case, the presence of these EDJs would require a modification of the medium description. With the presence of strong zonal jets, it is unclear if these mean flows produce these waves themselves or, vice versa, whether the jets are driven by waves [1]. The latter is suggested by the presence of wave attractors in the stratified-rotating equatorial region, which lead to repeated focusing and amplification of wave energy. These amplified waves may in turn lead to mixing of both density and angular momentum, which may lead to accelerating, eastward mean flows [9]. This is experimentally discussed in Maas 2001 [10].

2.1.1 Shallow water model

There are two models used to represent equatorial waves, the first one being the shallow water model. The approach assumes a thin layer of incompressible and homogeneous fluid ($N = 0$) of depth H' , the entire height of the fluid column, where a free surface $\eta(x, y, t)$ is considered. H' will be used for the height of the entire fluid column in the shallow water model to differentiate it from the depth used in the reduced gravity model, discussed in the next subsection. At the mean free surface ($z = 0$), the linearized kinematic and dynamic boundary conditions hold [1]:

$$p_{z=0} = g\eta \quad (2)$$

$$w_{z=0} = \eta_t, \quad (3)$$

which state that the pressure is constant across the interface and that once a particle is on the free surface, it will remain there. The shallow water model is a one layer approach to mathematically represent equatorial waves. The momentum equations of the linearized shallow water equations with the beta-plane approximation is [11]:

$$u_t - \beta y v = -g\eta_x \quad (4)$$

$$v_t + \beta y u = -g\eta_y \quad (5)$$

$$\eta_t + H'(u_x + v_y) = 0, \quad (6)$$

where $c'^2 = gH'$, which is the velocity of a travelling, long gravity wave, g is the gravitational constant 9.8 m/s^2 , and H' is typically the average depth of the ocean. c' is used for shallow water model speeds to differentiate it from reduced gravity model speeds. Using known, oceanic values gives a speed c' of $\approx 200 \text{ m/s}$, which is very fast for oceanic waves. One critique of the shallow water model is that it often gives higher approximations for velocity and spatial scales of oceanic waves, $c' = \mathcal{O}(10^2) \text{ m/s}$, for depths $H' = \mathcal{O}(10^3) \text{ m}$, which differs from observational evidence, which lists velocities $\mathcal{O}(1) \text{ m/s}$ [1]. Also, notice in the shallow water model that it assumes the fluid is barotropic, where the pressure depends only on the depth z (hydrostatic) surface elevation η of the fluid and acceleration due to the gravity. The one layer model representation may also appear too simplistic, especially regarding Kelvin waves whose meridional velocity goes to 0 [1].

This gives rise to a second, linear model known as the reduced gravity (or 1.5) layer model, which allows for more representation of the thermal and density structure of the equatorial ocean [1], [2].

2.1.2 Reduced gravity model (1.5 layer model)

The reduced gravity model (or 1.5 layer model) consists of the observed density structure of the equatorial ocean as a shallow layer of warm water above a layer of denser, colder water [12]. Figure 2 shows a visual diagram of the reduced gravity (1.5 layer) model. The two layers are separated by a thermocline, which allows ocean waves to propagate at the surface and in the interior along the thermocline interface. The second layer is assumed to be motionless (no zonal velocity) and also infinitely deep [1].

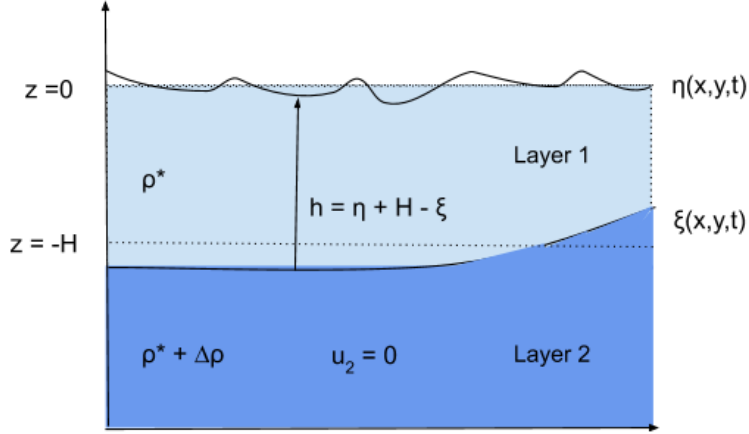


Figure 2: Reduced gravity model.

The mean position of the interface is at $z = -H$ and its dynamical position from the mean is described by $\xi(x, y, t)$. The thickness h for layer 1 in figure 2 of the reference density ρ_* is $h(x, y, t) = \eta(x, y, t) + H - \xi(x, y, t)$. The higher density is assumed for the second, infinitely deep layer, where the lower layer density is $\rho_* + \Delta\rho$. $\Delta\rho$ also signifies the density difference between the warmer, upper layer and the colder, lower layer. The second layer is also assumed to be motionless, so $u_2 = 0$. The hydrostatic equation for the second layer is as follows [1]:

$$\partial_z p_2 = -(\rho_* + \Delta\rho)g, \quad (7)$$

where p_2 is the pressure for the second layer. At the interface itself, two new boundary conditions hold which signify that the pressures at the interface equal each other and the change in interface depth with time is zero [11], [1]:

$$p_1(z = -H + \xi) = p_2(z = -H) \quad (8)$$

$$\frac{D(z + H - \xi)}{Dt}(z = -H + \xi) = 0. \quad (9)$$

In the first boundary condition, equation (8) the actual pressure ($p = p_0 + \tilde{p}$) appears, since the hydrostatic background pressure varies for each layer. p_0 is the average pressure, while \tilde{p} represents the small variations in pressure [1]. The second kinematic boundary condition, equation (9), states that at the interface, no particle will pass through the interface and the fluid will have zero velocity relative to the boundary. The relationship between sea surface height and the interface is established when evaluating the dynamic boundary condition, where the pressure in the second layer below the interface becomes:

$$p_2 = -g(\rho_* + \Delta\rho)(z + H - \xi) + \rho_*gh + p_{\text{atm}}. \quad (10)$$

Taking the horizontal gradient of equation (10), which should vanish as the second layer is motionless ($\vec{u}_2 = 0$), the equation becomes [1]:

$$\nabla_H \xi = -\frac{\rho_*}{\Delta\rho} \nabla_H \eta. \quad (11)$$

Equation (11) reiterates the fact that any small change in sea surface will result in an oppositely-signed change at the interface. This is valuable when comparing to observational sea level anomaly altimetry data as sea surface variations can be linked to thermocline elevation changes. When integrating the continuity equation vertically for the first layer from the interface to the sea surface, the equations resemble the shallow water equations but with $g\nabla\eta$ being replaced with $g'\nabla h$, where the reduced gravity is defined as:

$$g' = \frac{\Delta\rho}{\rho_*}g, \quad (12)$$

gravity times the ratio of maximum vertical density change and the reference density. The final form of the reduced gravity model, assuming the β -plane approximation and setting $f = 2\Omega \sin \phi$ to zero, is as follows:

$$u_t - \beta y v = -g' H \eta_x \quad (13)$$

$$v_t + \beta y u = -g' H \eta_y \quad (14)$$

$$\eta_t + (u_x + v_y) = 0, \quad (15)$$

$$\partial_t(\zeta - \beta y \eta) + \beta v = 0, \quad (16)$$

where η is still the free surface elevation and the relative vorticity is $\zeta = v_x - u_y$ [12]. Lastly, the speed of rotation-free longwaves, $c^2 = g'H$, with H is the depth of the mixed layer, typically 100 - 150 m, and g' is the reduced gravity, typically .02 m/s² [12]. Equation (16) is found by cross-differentiating and subtracting equations (13) and (14).

Assuming monochromatic, plane wave solutions:

$$\begin{bmatrix} u \\ v \\ \eta \end{bmatrix} = \begin{bmatrix} u(y) \\ v(y) \\ \eta(y) \end{bmatrix} e^{i(kx - \omega t)}.$$

Equations (13), (14), and (15) can be simplified to get one differential equation for one variable, where the u and η can be eliminated [11].

$$-\frac{\beta y}{c} \frac{\partial}{\partial t}(13) + \frac{1}{c} \frac{\partial^2}{\partial t^2}(14) - c \frac{\partial^2}{\partial y \partial t}(15) - c \frac{\partial}{\partial x}(16). \quad (17)$$

The factors before the partial derivatives in equation (17) are to eliminate all non- v terms. This simplifies down to:

$$\partial_t \left[\frac{1}{c^2} (v_{tt} + (\beta y)^2 v) - (v_{xx} + v_{yy}) \right] - \beta v_x = 0. \quad (18)$$

Now equation (18) is only dependent on the meridional velocity, v . Plane wave solutions can be assumed again, where:

$$v = \hat{v}(y) \exp[i(kx - \omega t)], \quad (19)$$

which can be summed into equation (20):

$$\hat{v}_{yy} + \hat{v} \left[\frac{\omega^2}{c^2} - k^2 - \frac{\beta k}{\omega} - \frac{\beta^2 y^2}{c^2} \right] = 0 \quad (20)$$

Equation (20) is homogeneous, and it is expected that nontrivial solutions that satisfy the latitudinally decaying, bounded condition will only exist for certain values of ω . However, before finding solutions to equation (20), the variables can be re-scaled where the time scale is $(1/2\beta c)^{1/2}$ and the length scale is $(c/2\beta)^{1/2}$ [8]. Keeping in mind that the length scale is equivalent to the equatorial Rossby radius of deformation:

$$R_{eq} = \text{Length scale} = \left(\frac{c}{2\beta} \right)^{1/2}. \quad (21)$$

For surface waves, the Rossby radius of deformation is comparable to 2000 km, while for internal waves it is about 100 km. After the scaling is inserted with ν representing the non-dimensional frequency and μ is the dimensionless wavenumber, the equation simplifies to [8]:

$$\hat{v}_{yy} + \hat{v} \left[\nu^2 - \mu^2 - \frac{\mu}{\nu} - y^2 \right] = 0. \quad (22)$$

Wave motions are near the equator where $y = 0$ and the boundary condition must be satisfied. This only occurs where $\hat{v} \rightarrow 0$, when $y \rightarrow \pm\infty$. Equation (22) and the boundary conditions pose an eigenvalue problem, where the boundary conditions are only satisfied when the frequency can be quantized and the solution will decay towards infinity [11]:

$$\nu^2 - \mu^2 - \frac{\mu}{\nu} = 2n + 1, \quad (23)$$

where $n = 0, 1, 2, 3, \dots$. Equation (23) is only valid for Hermite polynomials, else the Hermites explode when y in the re-scaled equation (63), becomes large or goes to ∞ .

The solution has the form of parabolic cylinder functions, which (when dimensionalized) is written as:

$$\hat{v}(y) = H_n \left(y \cdot \left(\frac{2\beta}{c} \right)^{1/2} \right) \cdot e^{-\beta y^2 / 2c} \quad (24)$$

where $H_n(y)$ is a Hermite polynomial of order n [12].

The dimensionalized, dispersion relation becomes [11]:

$$\frac{\omega^2}{c^2} - k^2 - \frac{\beta k}{\omega} = \frac{(2n + 1)\beta}{c}. \quad (25)$$

This gives way to the theoretical dispersion curve for equatorial waves:

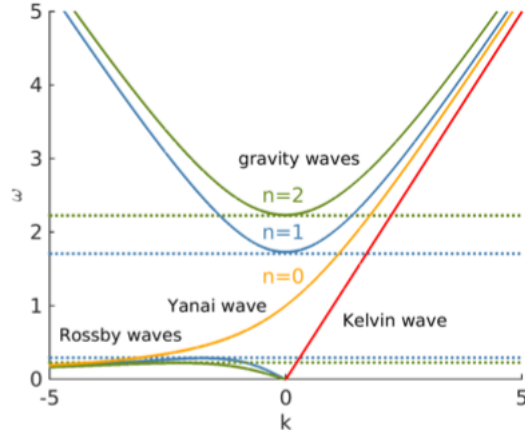


Figure 3: Dispersion curve for varying mode numbers (image of curve borrowed from [1]). The scale for the wave number k is $\sqrt{\beta/c}$ and frequency ω is $\sqrt{\beta c}$. Only waves with positive frequencies are shown. The dotted lines indicate the limiting frequencies for each mode number n [1].

2.1.3 Kelvin waves

The trivial solution, in which $\hat{v} = 0$, gives the solution for the equatorial Kelvin wave. Setting the meridional velocity v to zero, eliminating h , and integrating by separation of variables, gives the solution for $\hat{U}(y)$ to be:

$$\hat{U} = u_0 e^{-\beta y^2 / 2c}, \quad (26)$$

where u_0 is the amplitude of the perturbation zonal velocity at the equator [13]. The Kelvin wave is non-dispersive (see the red, straight line in figure 3), meaning that the phase speed is equal to the group speed of the wave energy for all frequencies and that this wave always propagates eastward [13]. For barotropic, surface Kelvin waves, (assuming the shallow water model, where the gravitational acceleration constant is taken into account rather than the reduced gravity):

$$c'^2 = gH', \quad (27)$$

where H' is the average depth of the ocean (4 km). The speed for surface, barotropic waves is approximately 200 m/s.

Meanwhile, for interfacial waves where the reduced gravity g' is used instead of g and a depth H of 150 m is assumed for equation 27, the speed of the Kelvin wave reduces down to 1.7 m/s (which also corresponds to the longwave internal wave speed):

$$c = \sqrt{g'H} = \sqrt{.002 \times 9.8\text{m/s}^2 \times 150\text{m}} = 1.7\text{m/s}. \quad (28)$$

The ratio between $\Delta\rho/\rho$ was estimated from density profiles for the Pacific, Atlantic, and Indian oceans by Pinault et al 2018 [14]:

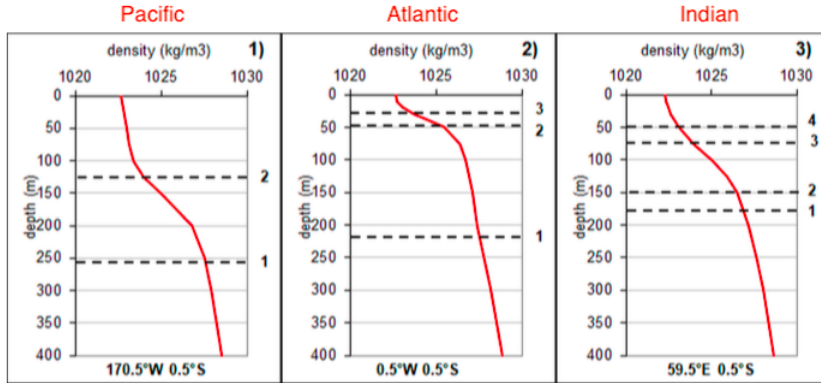


Figure 4: Density distributions for Pacific, Atlantic, and Indian ocean. Image from [14].

Figure 4 shows the density distributions at different locations close to the equator for the Pacific, Atlantic, and Indian ocean. The density difference between the top and bottom layer is determined by taking the difference between the two and then dividing by the average density of seawater (typically 1023 kg/m^3). The density difference between the two layers defined by the dashed lines, excluding the upper surface of the ocean (0 - 50m) as shown in the Atlantic ocean density profile, is around 2 kg/m^3 , which gives a density ratio of $\approx .002$.

Previous observational evidence in the equatorial Pacific has also pointed to Kelvin wave speeds for baroclinic mode 1 and 2 to be 2.5 - 2.9 m/s (period of 70 days) and 1.9 m/s (period of 120 days) [15]. The phase speed of 2.5 - 2.9 m/s depends on the depth and/or on the ratio between the densities of the mixed fluid: if the density difference is .005, rather than .002, then the speed becomes 2.8 m/s. Keep in mind that the long internal wave speed is referred to as c when considering the dispersion relation for different waves, while the phase speed (ω/k) will be referred to as c_p . The dispersion relation of equatorial Kelvin waves is:

$$\omega = kc_p, \quad (29)$$

where the phase speed $c_p = \omega/k$. The phase speeds and the dispersion relation are all positive, implying that Kelvin waves propagate solely in the eastward direction and are dispersionless.

2.1.4 Rossby waves

Referring to the original dispersion relation equation (25) and focusing on internal waves, if the ratio between the phase speed c_p and focusing internal wave speed (c) is very small:

$$\frac{\omega}{k} \frac{1}{c} = \frac{c_p}{c} \ll 1, \quad (30)$$

this allows for the dispersion relation for westward propagating Rossby waves:

$$\omega = \frac{-\beta k}{k^2 + (2n+1)\beta/c}, \quad (31)$$

Equation (31) can be rearranged for $c_p = \omega/k$:

$$c_p = \frac{\omega}{k} = -\frac{\beta}{k^2 + (2n+1)\beta/c}. \quad (32)$$

Notice that, unless k is very small compared to β/c , there is still a factor of k left in the denominator, implying that the phase speed must be dependent on the wavelength and hence that the wave is dispersive, where $k = 2\pi/\lambda$.

2.1.5 Gravity waves

The dispersion relation (25) for equatorially trapped waves can be written as:

$$\omega^2 \approx \beta c(2n + 1) + (kc)^2, \quad (33)$$

assuming that the β parameter is much smaller than ωk and thus frequency values dominate resulting in the ratio of β/ω being small.

Equation (33) can be reduced even further by assuming that the squared frequency ω^2 is much greater than $(kc)^2$, which also implies that the wavelength λ must be very large, as the wavenumber and wavelength are inversely proportional:

$$\omega^2 \gg (kc)^2 \rightarrow c_p = \frac{\omega}{k} \gg c, \quad (34)$$

where c^2 is proportional to the wavelength λ^2 .

This reduces the gravity wave dispersion relation to:

$$\omega^2 \approx (2n + 1)\beta c. \quad (35)$$

There is no longer the presence of the wave number in this reduction anymore, which implies that the frequency is the same for any wave number.

2.1.6 Mixed Rossby-gravity waves

Provided that the ratio c_p/c is equal to -1 and the mode number is 0, this results in the dispersion relation for mixed Rossby gravity waves:

$$\omega_{\pm} = \frac{1}{2}kc \pm \left[\frac{1}{4}k^2c^2 + c\beta \right]^{1/2}. \quad (36)$$

Assuming that $4c\beta/k^2c^2$ is much smaller than one, the term in the square root of equation (36) can be simplified using the Taylor approximation: $(1 + x)^p \approx 1 + px$, where $(\frac{1}{4}k^2c^2 + c\beta)^{1/2}$ can be re-written as:

$$\left[\frac{1}{4}k^2c^2 + c\beta \right]^{1/2} = \frac{kc}{2} \left(1 + \frac{4c\beta}{k^2c^2} \right)^{1/2} \approx \frac{kc}{2} \left(1 + \frac{2c\beta}{k^2c^2} \right). \quad (37)$$

The approximated dispersion relation can be re-written as:

$$\omega_{\pm} \approx \frac{1}{2}kc \pm \frac{1}{2}kc \left(1 + \frac{2\beta}{k^2c} \right). \quad (38)$$

Looking at the approximated ω_- , the dispersion relation becomes $\omega_- \approx -\beta/k$, which is in agreement with the Rossby wave solution. This stems from the approximated gravity wave dispersion relation, equation (35), in the limit that when dividing both sides by c^2 , the squared wavenumber k^2 is much larger than $\beta(2n + 1)/c$.

Focusing on the negative root of the non-approximated dispersion relation of equation (36), and assuming that $(k^2c^2)/4 \ll c\beta$, the frequency becomes: $\omega_- \approx -\sqrt{c\beta}$. This is in agreement with the long-wave limit of the gravity wave solution.

The phase speed, from the dispersion relation, can then be determined for $c_p = \omega/k$:

$$c_p = \frac{\omega}{k} \approx \frac{c}{2} \left[1 \pm \left(1 + \frac{2\beta}{k^2 c} \right) \right] \quad (39)$$

Observations made of westward propagating MRG wave speeds in the Western Equatorial Pacific region are shown to be about -3.6 m/s with an approximate wavelength of 4,000 km [16]. There were also observations of westward MRG waves in the equatorial Atlantic by Weisberg et al 1979, at a period of 30 days, wavelength of 1220 km, and speed of -.45 m/s [17].

In all the dispersion relations and phase speeds for different wave types using the traditional, β -plane approximation, speeds are contingent on the wave number and in turn the wavelength. The wavelength can be determined when comparing to observational data, which will be discussed more in the results section.

The two models, shallow water and reduced gravity model, show clear differences. The reduced gravity model provides phase speeds and spatial scales that are more reasonable in comparison to observational evidence, while shallow water values highly overestimate [1]. However, the use of the reduced gravity model mandates some assumptions that may not be applicable to the equatorial region. For example, it is based on the assumption of an infinitely sharp thermocline and motionless lower layer which clashes with the known presence of zonal EDJs. Lastly the interior dynamics with the upper, mixed layer are ignored when regarding the equations of motion as depth integrated relations over the whole layer [1].

2.2 Coriolis Force

It may be useful to first unpack the Coriolis force and its proceeding components, as the Coriolis force components are the driving factor for the non-traditional approach.

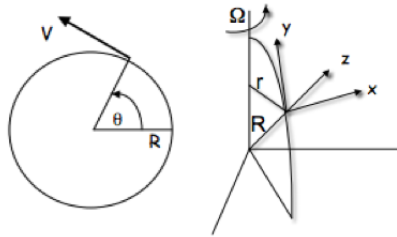


Figure 5: Cylindrical coordinate system, where R is the radius of the earth. r is the particle's distance, Ω is earth's rotational axis, and V is the tangential velocity of the rotating earth [18].

The angular speed Ω can be defined as:

$$\Omega = \frac{d\theta}{dt} = V/R, \quad (40)$$

where R is the radius of the earth, and V is the tangential velocity [18]. Points along the radius R and the angular speed can be defined as:

$$\vec{R} = [x\hat{i}, y\hat{j}] = R[\cos(\theta t)\hat{i}, \sin(\theta t)\hat{j}],$$

$$\vec{\Omega} = \Omega\hat{k}.$$

The position vector can be defined as:

$$x = R \cos(\theta t), y = R \sin(\theta t). \quad (41)$$

The cross product between the position and rotation vector is:

$$\vec{\Omega} \times \vec{R} = \begin{bmatrix} \hat{i} & \hat{j} & \hat{k} \\ 0 & 0 & \Omega \\ R \cos(\theta t) & R \sin(\theta t) & 0 \end{bmatrix} = \Omega R [-\sin(\theta t)\hat{i}, \cos(\theta t)\hat{j}] = V [-\sin(\theta t)\hat{i}, \cos(\theta t)\hat{j}].$$

The distance vector \vec{R} can be defined as:

$$\vec{R} = x\hat{i} + y\hat{j} + z\hat{k}. \quad (42)$$

Taking the time derivative of equation (42) (keeping in mind that the time derivative of a variable will be in the dot notation \dot{x}):

$$\frac{d\vec{R}}{dt} = \underbrace{\left(\frac{dx}{dt}\hat{i} + \frac{dy}{dt}\hat{j} + \frac{dz}{dt}\hat{k} \right)}_{\dot{R}} + \underbrace{\left(x \frac{d\hat{i}}{dt} + y \frac{d\hat{j}}{dt} + z \frac{d\hat{k}}{dt} \right)}_{\vec{\Omega} \times \vec{R}}. \quad (43)$$

\dot{R} shows the rate of change relative to a fixed reference point, while $\vec{\Omega} \times \vec{R}$ is the rate of change of a reference point relative to the earth's center [18]. The rate of change the vector \vec{R} can be re-written as:

$$\frac{d\vec{R}}{dt} = \dot{R} + \vec{\Omega} \times \vec{R}. \quad (44)$$

Taking another time derivative of $\frac{d\vec{R}}{dt}$ is:

$$\frac{d}{dt} \frac{d\vec{R}}{dt} = \frac{d\dot{R}}{dt} + \frac{d}{dt}(\Omega \times R). \quad (45)$$

The product rule can then be taken and equation (44) can be plugged in for $\frac{dR}{dt}$:

$$\begin{aligned} \frac{d}{dt} \frac{d\vec{R}}{dt} &= \frac{d\dot{R}}{dt} + R \times \frac{d\Omega}{dt} + \Omega \times \frac{dR}{dt} \\ &= \frac{d}{dt}(\dot{R} + \Omega \times R) + \Omega \times (\dot{R} + \Omega \times R) \\ &= \ddot{R} + \dot{\Omega} \times R + \Omega \times \dot{R} + \Omega \times (\dot{R} + \Omega \times R). \end{aligned}$$

$\dot{\Omega}$ can be eliminated because the angular speed of rotation does not vary in time:

$$\frac{d}{dt} \frac{d\vec{R}}{dt} = \ddot{R} + 2\Omega \times \dot{R} + \Omega \times (\Omega \times R). \quad (46)$$

\ddot{R} can be interpreted as the acceleration relative to a fixed point on the earth's surface, and $2\Omega \times \dot{R} + \Omega \times (\Omega \times R)$ is the acceleration of a fixed point on the surface of the earth [18]. The last term in equation (46):

$$\Omega \times (\Omega \times R) \approx 0, \quad (47)$$

represents the centrifugal force, which is small in magnitude and depends on the rotation rate and the radial distance from the rotation axis. The centrifugal force is typically regarded as unimportant, so it can be absorbed in the pressure [12], which results in:

$$\frac{d}{dt} \frac{d\vec{R}}{dt} = \ddot{R} + 2\Omega \times \dot{R}, \quad (48)$$

where $2\Omega \times \dot{R}$ can be simplified. From equation (42), the \dot{R} (observed velocity) can be written as:

$$\dot{R} = \vec{U} = u\hat{i} + v\hat{j} + w\hat{k}, \quad (49)$$

and $\vec{\Omega}$, the angular velocity vector, is defined as:

$$\vec{\Omega} = \Omega \cos \phi \hat{j} + \Omega \sin \phi \hat{k}. \quad (50)$$

$2\Omega \times \dot{R}$ can be simplified to:

$$2\Omega \times \dot{R} = \begin{bmatrix} \hat{i} & \hat{j} & \hat{k} \\ 0 & 2\Omega \cos \phi & 2\Omega \sin \phi \\ u & v & w \end{bmatrix} = 2\Omega [(w \cos \phi - v \sin \phi)\hat{i} + u \sin \phi \hat{j} - u \cos \phi \hat{k}]. \quad (51)$$

\ddot{R} can be defined as:

$$\ddot{R} = \frac{du}{dt} \hat{i} + \frac{dv}{dt} \hat{j} + \frac{dw}{dt} \hat{k}. \quad (52)$$

The classic, Coriolis parameter is defined as $f = 2\Omega \sin \phi$, and the "reciprocal" Coriolis parameter is defined as $\tilde{f} = 2\Omega \cos \phi$ [12]. Putting it all together results in the full Coriolis term, which can later be simplified to represent the full equations of motion:

$$\frac{d^2 R}{dt^2} = [\dot{u} + \tilde{f}w - fv]\hat{i} + [\dot{v} + fu]\hat{j} + [\dot{w} - \tilde{f}u]\hat{k}. \quad (53)$$

The complete Coriolis force exemplifies the primary difference between the traditional and non-traditional approach, as the non-traditional equations of motion include a holistic view of the Coriolis force.

2.3 Nontraditional approximation

We can now start by including the non-traditional Coriolis component into the equations of motion. The hydrostatic approximation is still assumed, but the nontraditional component of the Coriolis force is retained, where $\tilde{f} = 2\Omega \cos \phi \approx 2\Omega$ and $f = 2\Omega \sin \phi \approx 2\Omega y/a = \beta y$. The following derivations of equatorial waves using the nontraditional component is from Anna Rabitti's doctoral thesis [1], Maas et al 2007 [9], and Maas 2016 [19]. The non-hydrostatic, non-traditional set of equations is written in vectorial format, where [1]:

$$\vec{\Omega} = \Omega(\hat{e}_y + \frac{y}{a}\hat{e}_z) \quad (54)$$

$$\vec{u}_t + 2\vec{\Omega} \times \vec{u} = -\nabla p \quad (55)$$

The curl can then be taken, which yields the vorticity balances [1]:

$$\nabla \times (\vec{u}_t + 2\Omega(\hat{e}_y + \frac{y}{a}\hat{e}_z) \times \vec{u} + \nabla \times \nabla p = 0, \quad (56)$$

where the curl of the gradient of p is zero and $\beta = 2\Omega/a$. The curl of $2\vec{\Omega} \times \vec{u}$ is approximated as:

$$2\vec{\Omega} \times \vec{u} = \begin{bmatrix} \hat{e}_x & \hat{e}_y & \hat{e}_z \\ 0 & 2\Omega & 2\Omega y/a \\ u & v & w \end{bmatrix} = 2\Omega[(w - \frac{y}{a}v)\hat{e}_x + \frac{y}{a}u\hat{e}_y - u\hat{e}_x], \quad (57)$$

where equation (56) can be re-written as:

$$(\nabla \times \vec{u})_t + \beta v \hat{e}_z - 2\Omega L \vec{u} = 0. \quad (58)$$

The operator L is $L = \partial_y + \frac{y}{a}\partial_z$. The curl of equation (58) can be taken again, using the continuity equation $\nabla \cdot \vec{u} = 0$ and recalling that by assuming monochromatic waves, $\propto \exp(-i\omega t)$, the partial time derivatives ∂_t can be converted to $-i\omega$ [1]:

$$i\omega \Delta \vec{u} + \beta \begin{bmatrix} v_y - w_y \\ -v_x \\ u_z \end{bmatrix} - \frac{2\Omega}{i\omega} L \begin{bmatrix} 0 \\ 0 \\ \beta v \end{bmatrix} + \frac{4\Omega^2}{i\omega} L^2 \begin{bmatrix} u \\ v \\ w \end{bmatrix} = 0. \quad (59)$$

The operator L^2 can be expanded out as:

$$L^2 = (\partial_y + \frac{y}{a}\partial_z)^2 = \partial_y^2 + 2\frac{y}{a}\partial_z\partial_y + (\frac{y}{a})^2\partial_z^2 + \frac{1}{a}\partial_z. \quad (60)$$

Notice in equation (59), when the matrices are completely expanded for each zonal, meridional, and vertical velocity component, the meridional velocity v has no dependence on any other variable. For example when equation (59) is expanded, u and w both have dependence on other velocity components. Rabitti assumes all the quantities to be proportional to e^{ikx} , where the partial x -derivative can be replaced with ik . The frequency can also be normalized where $\omega' = \frac{\omega}{2\Omega}$ and the primes are dropped [1]:

$$[-((\omega k)^2 + \frac{\omega k}{a}) + (\omega^2 - 1)\partial_y^2 + (\omega^2 - \frac{y^2}{a^2})\partial_z^2 - 2\frac{y}{a}\partial_y\partial_z - \frac{1}{a}\partial_z]v = 0. \quad (61)$$

Equation (61) will contain oscillatory solutions provided that it is of a hyperbolic type, which will occur only if $\omega < 1$ [1]. It can also be re-scaled to set the ∂_y^2 in L to one:

$$(k, l) = \frac{1}{a}(k', l'), y = a\sqrt{1 - \omega^2}y', (y, z) = a \cdot (x', z'), t = \frac{1}{2\Omega}t'. \quad (62)$$

The primes can be dropped and equation (61) can be converted to [1]:

$$[-\omega k(1 - \omega k) - \partial_y^2 + (\omega^2 - (1 - \omega^2)y^2)\partial_z^2 - 2y\partial_y\partial_z - \partial_z]v = 0. \quad (63)$$

Notice this equation is similar to the non-stratified Stern equation [9], but it is extended in that there are extra factors of ω and k . In order to find solutions for this second order PDE equation (63), observe that the linear PDE in two independent variables has the form:

$$Ad_{yy} + 2Bd_{yz} + Cd_{zz} + \text{lower order terms} = 0. \quad (64)$$

The variables A, B, and C for equation (63) are:

$$A = -1, B = -y, C = \omega^2 - (1 - \omega^2)y^2, \quad (65)$$

where $\delta = AC - B^2 = -\omega^2(1 + y^2) < 0$ [1]. The equation is hyperbolic for all values of y provided that $\omega < 1$. The relation to determine the two characteristics is:

$$\frac{dz}{dy} = \frac{B \pm (-\delta)^{1/2}}{A} = y \pm \omega(y^2 + 1)^{1/2}. \quad (66)$$

Through separation of variables, a new coordinate can be introduced [1]:

$$z - \int \frac{B \pm (-\delta)^{1/2}}{A} dy = \chi_{\pm}, \quad (67)$$

where the PDE form can now be described as:

$$\partial_{\chi_+} \partial_{\chi_-} v + \dots = 0, \quad (68)$$

where only a mixed derivative appears. However the mixed derivative can be removed by introducing [1]:

$$\hat{\xi} = \chi_+ + \chi_- = 2z - 2 \int \frac{B}{A} dy = 2x - y^2 \quad (69)$$

$$\hat{\eta} = \chi_+ - \chi_- = -2 \int \frac{(-\delta)^{1/2}}{A} dy = \omega y(y^2 + 1)^{1/2} + \omega \ln(2(y^2 + 1)^{1/2} + y). \quad (70)$$

Notice that in equation (70), there is only y -dependence and it is a rather long way of describing a coordinate, which calls for a more convenient way of re-expressing coordinates [1]:

$$\xi = z - \frac{y^2}{2} \quad (71)$$

$$\eta = y. \quad (72)$$

Equation (63) can be now written with the change in coordinates:

$$[\omega k(1 + \omega k) + \partial_{\eta}^2 - \omega^2(1 + \eta^2)\partial_{\xi}^2]v = 0. \quad (73)$$

Applying all the manipulations to equation (59) and applying the continuity equation to replace w_z results in:

$$(-\omega^2 k^2 + \omega^2(1 + \eta^2)\partial_{\xi}^2 - \partial_{\eta}^2) \begin{bmatrix} u \\ v \\ w \end{bmatrix} - i\omega \begin{bmatrix} (\frac{2}{\sqrt{1-\omega^2}}(v_{\eta} - \eta v_{\xi}) + iku) \\ -ikv \\ u_{\xi} \end{bmatrix} + \begin{bmatrix} 0 \\ 0 \\ (\frac{1}{\sqrt{1-\omega^2}}(v_{\eta} - \omega^2 \eta v_{\xi})) \end{bmatrix} = 0. \quad (74)$$

When expanding out the matrices, the u -equation appears to be a forced version of the v -equation [1]. Taking the equation for v alone results in:

$$(-\omega^2 k^2 + \omega^2(1 + \eta^2)\partial_{\xi}^2 - \partial_{\eta}^2)v - \omega kv = 0. \quad (75)$$

Equation (75) can be solved by converting it to a Hermite's differential equation through a separation ansatz $v = e^{l\xi}V(\eta)$ [1]:

$$[\omega k(1 + \omega k) + \partial_\eta^2 - \omega^2(1 + \eta^2)l^2]V(\eta) = 0, \quad (76)$$

where $V = e^{-\omega l \eta^2/2} \mathcal{H}(\sqrt{\omega l} \eta)$, where Hermite's equation now holds (provided $n = 0, 1, 2, 3, \dots$):

$$\mathcal{H}_n'' - 2\sqrt{\omega l} \eta \mathcal{H}_n' + 2n \mathcal{H}_n = 0, \quad (77)$$

and the dispersion relation can be written as:

$$2n + 1 = \frac{\omega}{l} \left(k^2 - l^2 + \frac{k}{\omega} \right) \quad (78)$$

$$\text{Dimensionalized} \rightarrow \omega_n = -\beta \frac{k - l(2n + 1)}{k^2 - l^2}. \quad (79)$$

Only solutions where n is an integer can be accepted, as any other solution will explode for $y \rightarrow \pm\infty$ also where $k = l$ which corresponds to $n = 0$. From the separation ansatz and change of coordinate, the factor l is an inverse decay scale in the negative $z - y^2/2$ direction, rather than a wavenumber as the ansatz lacks a factor of the imaginary number i . This can be pictured as a parabola folded around the equator, with the global minima exactly 0° in latitude. The phase speed can also be computed by multiplying both sides of equation (79) with the inverse zonal wavenumber:

$$c_p = \frac{\omega}{k} = -\frac{\beta}{k} \left(\frac{k - l(2n + 1)}{k^2 - l^2} \right). \quad (80)$$

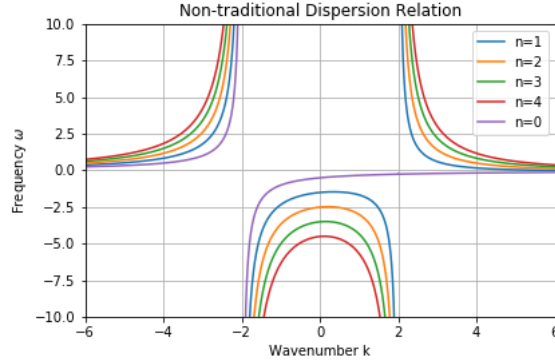


Figure 6: Dispersion relation for non-traditional approach, with $l = 2$ [1].

Figure 6 shows the dispersion curve of the non-dimensionalized zonal wavenumber and frequency, assuming $l = 2$. It is visually very different from the classical dispersion relation, figure 3, besides there being an extra dependence on the variable l , where l is an inverse decay scale in the negative $z - y^2/2$ direction. There is also an asymmetry under the sign reversal of $\pm k$, which is especially visible for mode number $n = 0$. Singularities also occur in the dispersion relation whenever $l = k$.

Equation (79) appears almost even simpler than the traditional approximation and resembles the classical dispersion relation for Rossby waves [1]. Assuming zonal symmetry (the wavenumber k is set to zero), and the case of low frequencies, equation (79) reduces to:

$$\omega_n = -\beta \frac{2n+1}{l}. \quad (81)$$

Equation (81) resembles $\omega = -\beta/k$, provided that the mode number $n = 0$. There is a non-trivial z dependency in the solutions for u, v, w , also shown with the vertical wave number dependence, while in traditional theory, it is only the vertical velocity that is dependent on z . This in turn implies that it is not possible to connect different equatorial wave solutions by taking certain limits [1]. It is interesting how adding the horizontal component of the Coriolis force creates an entirely different view of wave propagation with dependencies not only on the zonal wavenumber but also the inverse decay scale.

2.3.1 Presence of eastward Rossby waves

The equatorial boundary layer may allow for the existence of a special type of Rossby wave. Assume an idealized ocean covers the entire planet between two concentric spheres of dimensionless radii 1 and $R < 1$ [19], picture a spherical shell of water. The arguments made here are drawn from Maas 2016 [19]. The focus of this idealized oceanic situation is for topographic Rossby waves, but topographic Rossby waves (TRW) can be linked to planetary Rossby waves. The constant, dimensional depth H^* of the idealized ocean shows that the radius of the inner sphere is:

$$R = 1 - H^*/a, \quad (82)$$

where a is the earth's radius and H^* becomes dimensionless as it is divided by a . In cylindrical coordinates (r, λ, z) , z is the axial distance from the equatorial plane, r is the distance from the rotation axis Ω , and λ is the zonal coordinate [19].

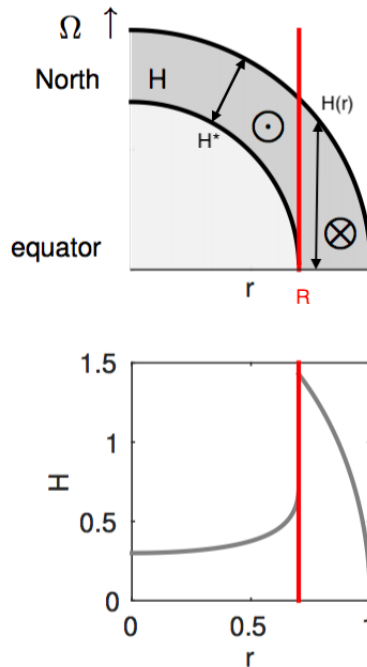


Figure 7: The top figure shows the meridional view of the thickness of the aquaplanet (gray shading) in the northern hemisphere. The rotation axis is perpendicular to the radius r , H is the height of the fluid layer parallel to the rotation axis [1], and H^* is the mean, constant depth of the layer between the two radii. R represents the radius to the inner shell. The lower figure shows the height of fluid column (H) decreasing rapidly as a function of cylindrical radial distance. Image borrowed from [1] and [19].

The top panel of figure 7 shows the setup of a quarter of a sphere with the idealized ocean in gray. The boundaries are assumed to be fixed and thus gravity does not affect the internal fluid motions [19]. While the ocean depth H^* is a constant, the depth $H(r) = H_o(r) - H_i(r)$ as measured parallel to the rotation axis is important to consider as the fluid column changes with height as one moves further away from the parallel rotation axis [19]. When $r > R$, this is equivalent to:

$$H(r) = 2H_o(r) = 2(1 - r^2)^{1/2}, \quad (83)$$

where H_o is the height of the fluid column between the equatorial plane and the outer sphere. Similarly, $H_i = \sqrt{R^2 - r^2}$ is the height of the column above the equatorial plane up to the inner sphere at cylindrical radius r .

Looking at the lower panel of figure 7, the axial depth H appears to be increasing slowly as the radial distance increases, but at $r = R$, there is a large jump in axial depth. This large jump occurs at a latitude of $\approx 1.97^\circ$ [19]:

$$\phi_e \approx \tan \phi = \frac{H_o(R)}{R} = \frac{(1 - R^2)^{1/2}}{R} \approx \left(\frac{2H}{a}\right)^{1/2} \approx 1.97^\circ. \quad (84)$$

The region in between the latitude $\pm\phi_e$, or for any radii greater than R , is called the equatorial region, where from the bottom picture of figure 7, $H(r)$ decreases rapidly as r increases, vanishing at

the equatorial surface. This axial ocean depth $H(R)$, or the depth measured parallel to the rotation axis at the radius of the tangent cylinder, is on the order of 400 km [19]. This depth is much smaller than the length of oceanic basins, which is on the order of 4000 km. The difference in height and length allows the assumption of the small aspect ratio $\delta = H/L$ to still hold, which is the basis for TRW theory.

For $r < R$, the radial depth decreases towards the rotation axis, $r = 0$, as seen in the bottom panel of figure 7. It can be inferred that topographic Rossby waves propagate westward. Changes in the bottom topography can result in the generation of low frequency waves, much like planetary Rossby waves [20]. When considering potential vorticity changes with the Coriolis parameter (dependent on latitude) and water depth, the PV considerations indicate that shallower fluid depths correspond to higher latitudes implying that topographic waves will propagate with shallow depths to their right seen from their direction of propagation [20]. This is very similar to the westward propagation of planetary Rossby waves under the influence of the changing Coriolis parameter.

This can be shown in the upper panel of figure 7, outside the equatorial band, $r < R$, TRWs propagate westward (pointing out of the page), while inside the equatorial band, TRWs are expected to propagate eastward (pointing into the page) [1], [19].

Planetary Rossby waves can be compared to TRWs when looking at the geometry. In the TRW case, the planetary vorticity (2Ω) is constant. At the latitude where the cylindrical radius $r = R \cos \phi$, $H(r)$, the axial depth equals [19]:

$$H(R \cos \phi) = a(H_0 - H_i), \quad (85)$$

which changes gradually. For constant, radial depths of the shell ($H^* \ll a$), in polar and mid-latitude regions, the depth can be approximated as:

$$H \approx \frac{H^*}{\sin \phi}. \quad (86)$$

This expression resonates with the traditional expression for planetary potential vorticity $2\Omega/H = 2\Omega \sin \phi/H^* = f/H^*$. Along the equator, where the latitude is close to 0° , expansions of the expression for the background PV lead to either a non-uniformity in H or f [19]. Topographic Rossby waves in the mid and higher latitude regions of a spherical shell appear to explain the existence of planetary Rossby waves based on the re-written description of planetary vorticity to background potential vorticity. These non-traditional TRWs are termed columnar inertial modes, where the phase speeds are obtained by following Maffei 2017 [21].

Maffei 2017 discusses the interior dynamics when considering fluid filled spheroidal containers, similar to the aquaplanet theorized before. The quasi-geostrophic approximation is assumed where horizontal flows have a columnar structure, no change in the vertical direction [21]. We will give a summary of their results.

A rotating sphere of radius a can be pictured whose axis of rotation ($\vec{\Omega}$) passes through the center of the sphere. Inviscid flow is assumed, and the momentum equations are:

$$\vec{u}_t + 2\hat{e}_z \times \vec{u} + \nabla p = 0. \quad (87)$$

The velocity $\vec{u}(s, \phi, z)$ can be re-written in terms of cylindrical coordinates and the stream function, where ϕ is the longitude, θ is co-longitude, $s = r \sin \theta$, and $z = r \cos \theta$: [21]. Time and distance are scaled with Ω^{-1} and a .

$$\vec{u}(s, \phi, z) = \frac{1}{H} \nabla \times (\Psi(s, \phi) \hat{e}_z) - \frac{sz}{H^2} u_s(s, \phi) \hat{e}_z, \quad (88)$$

where $H = \sqrt{1 - s^2}$ and followed by the impermeable wall boundary condition $\Psi(s = 1) = 0$ [21]. An ansatz can be made when considering normal mode solutions, in terms of \vec{u} or the stream function Ψ , where m is the azimuthal wavenumber and ω is the angular frequency:

$$\vec{u}(s, z, \phi, t) = \hat{u}(s, z) \exp(i(m\phi + \omega t)) \quad (89)$$

$$\Psi(s, \phi, t) = \hat{\Psi}(s) \exp(i(m\phi + \omega t)). \quad (90)$$

Notice that the ansatz for both \vec{u} and Ψ is the positive ωt ; this implies that all negative zonal wave numbers will represent eastward propagation or conversely, for all positive azimuthal wave numbers, eastward propagation will occur when frequencies are negative. The curl can be taken of equation (87) in order to eliminate the pressure gradient and consider the axial vorticity equation. The vertical component of the resulting equation is [21]:

$$\left[\partial_s \left(\frac{s}{H} \partial_s \right) + \frac{1}{sH} \partial_\phi^2 \right] \Psi_t - 2 \frac{s}{H^3} \Psi_\phi = 0. \quad (91)$$

Equation (91) results in the axial vorticity equation, where now the ansatz (equation (90)) can be used. By considering the non-permeable boundary condition, an eigenvalue problem is obtained for the radial function $\hat{\Psi}$ [21]:

$$\omega \left[\frac{d}{ds} \left(\frac{s}{H} \frac{d}{ds} \right) - \frac{m^2}{sH} \right] \hat{\Psi} - 2n \frac{s}{H^3} \hat{\Psi} = 0, \quad (92)$$

where n is given by integer numbers where $n = 1, 2, 3, \dots$. The non-dimensionalized dispersion relation is given by:

$$\omega_n = - \frac{m}{n(2n + 2m + 1) + m/2}, \quad (93)$$

which assumes the geometry of a 2D disk with no vertical extension, rather than a spherical shape. In order to account for a spheroidal shape, the parameter b which is the semi-minor axis in an oblate spheroid of equatorial radius s can be introduced into the dispersion relation:

$$\omega_n = - \frac{m}{n(2n + 2m + 1) + m/2 + (mb)^2/6}, \quad (94)$$

The dispersion relation from equation (94) with wavenumber on the x-axis and frequency on the y-axis is represented graphically:

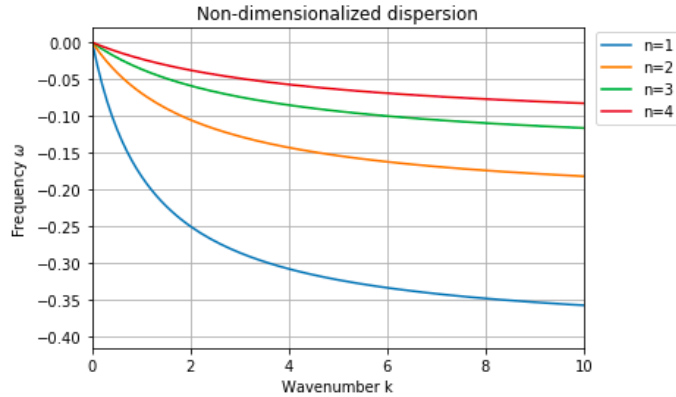


Figure 8: Non-dimensionalized dispersion relation for columnar flow, where negative frequencies indicate eastward propagation.

The frequencies are negative, which indicates eastward wave propagation as the ansatz assumes a positive zonal wave number and frequency. The dispersion relation shows the parameter $b = 1$, which indicates a spherical shape [21].

The dimensionless phase speed can be found from the dispersion relation by dividing equation (94) by the azimuthal wavenumber m , where ϕ and thus m is still dimensionless. The scaling for distance and time, the dimensional phase speed is:

$$c_p = -\frac{\Omega}{n(2n + 2m^* + 1) + m^*/2 + (m^*b)^2/6}, \quad (95)$$

where the dimensional, azimuthal wavenumber is described as: $m^* = 2\pi a \cos \phi / \lambda_x$, a being the radius of the earth, ϕ is the latitude (taken to be zero for the equatorial region), and λ_x being the zonal wavelength. Similar to the traditional phase speeds, the dispersion relation is contingent on the zonal wavelength and thus the azimuthal wavenumber.

3 Observational data and pre-processing

3.1 Sea level anomaly data

Now that obtaining the phase speeds of equatorial waves has been reviewed from the theoretical perspective, there is motivation to investigate any connections with observational data to obtain a more holistic viewpoint of the equatorial boundary layer. Sea surface height or sea level anomaly (SLA) altimetry data was used, consisting of merged data taken from different altimeter missions (L4 level) at a $.25^\circ$ resolution. The data is taken from *Copernicus*, Marine Environment Monitoring Service. As the equatorial region expands the entire circumference of the globe, three different oceans were looked at: Atlantic, Indian, and Pacific.

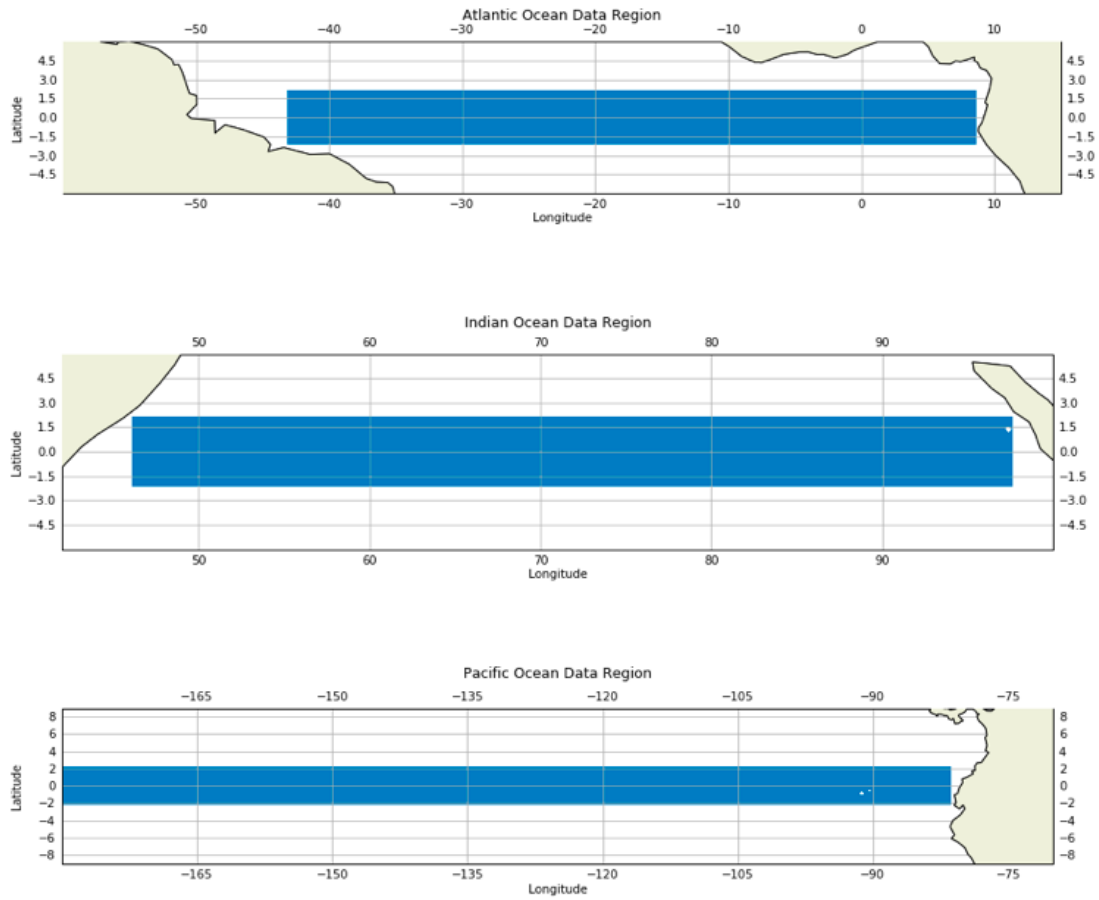


Figure 9: First panel shows the Atlantic ocean geographical region, second panel shows the Indian ocean, and third panel shows the Pacific ocean extent.

Each geographical region extends from $\pm 2^\circ$ in latitude. Notice for the top panel showing the Atlantic ocean extent, the blue strip does not extend all the way to the coast around 50°W , first due to there being issues with masked values in the data array, especially when taking the 2D Fourier transform. Looking at the first panel showing the Atlantic ocean, just off the coast of Brazil, there is the Amazon basin where there is an estuary from the Amazon river to the Atlantic ocean. That region is known to have a high amount of turbulence, which could be seen from the altimetry data. The high amount of turbulence, if included, may create false spectral peaks when performing the spectral analysis, which is why that region is masked out.

3.2 Pre-processing

The raw SLA signal was preprocessed before performing any Fourier analyses on it. The signal was first detrended by subtracting the mean, in order to make the signal resemble periodic, thus limiting any power spectral density anomalies that may occur due to there being a trend in the data. Then the detrended SLA signal was divided by the standard deviation to standardize the data.

A tapering function was applied which tapered the segments of the data to zeros at the end to ensure the connecting points are smoother of a finite time series, thus reducing any false spectral peaks that might arise from a discontinuity at the beginning and end of the time series.

Three different tapering functions were investigated. The first was adding extra zeros to the ends of the time series to make the ends of the signal continuous. The second was imposing zeros at the end of the time series, so cutting the ends off and reducing them sharply to reach zero. The third tapering was adding half sines to the ends of the taper:

$$\text{Half sine taper} = \frac{1}{2} \sin\left(\frac{\pi n}{N}\right), \quad (96)$$

where n is defined as the array from 0 to the desired taper length, and N is the full length of the time series [22]. The taper length was made to be approximately 3 percent of the time series:



Figure 10: Half sine taper over time showing for only two years (2018 - 2019) at one spatial location in the Atlantic ocean.

The half sine taper was selected as the taper of choice before performing any spectral analysis because with imposed zeros added to the ends of the time series, there showed to be an elevated power spectrum by a factor of 10. This is most likely due to the abrupt drop to zeros if the ends of the particular time series are not close to a standardized SLA of zero. The zero padding and the half sine taper showed the same power spectrum magnitude but adding additional zeros calls for caution if looking at the phase, since the time series length is extended from the original one. The next section consists of the results from the observational data and the observed phase speeds, where the appendices A - C explain in further details the technicalities behind the methods used.

4 Results

4.1 Spectral analysis

The 1D spectral analysis was done for the Atlantic, Indian, and Pacific ocean regions. The 1D Fourier transform was taken over the entire time series from 1993 to the end of 2019 after de-trending and tapering the ends of each time segment. After the FT was taken, the power spectrum was computed by taking the absolute square of the FT divided by the total number of samples. The logarithm of the power spectrum was taken to facilitate easier visualization of the peaks in the power spectrum.

The goal of finding the power spectrum is to determine what periods/frequencies correspond to the higher and lower power spectrum magnitudes as a function of frequency.

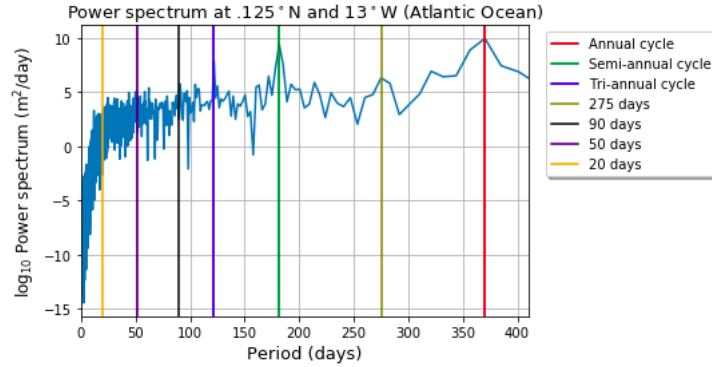


Figure 11: Power spectrum of Atlantic Ocean time series (1993 - 2019).

Figure 11 shows the power spectrum for the Atlantic Ocean at one spatial location: 125°N and 13°W . The period vs logarithmic scale of the power spectrum is plotted. The annual cycle at 360 days, marked by the red vertical line, is dominant period to the power spectrum. The semi-annual and tri-annual follow suit in preceding order to the power spectrum magnitude. The annual cycle is most dominant, even though the sun passes overhead twice per year leading to a strong semi-annual variation in the solar forcing. The annual cycle is thought to be due to ocean-atmosphere interactions between sea surface winds and sea surface temperature changes [23]. There appears to be an decrease in power spectrum values for higher frequencies/shorter periods as the 1D Fourier transform divides time varying sea level anomalies into an approximated sum of sinusoidal functions with increasingly high frequency.

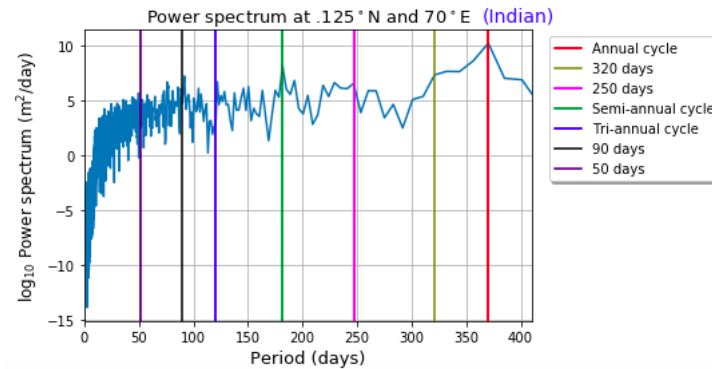


Figure 12: Power spectrum of Indian Ocean time series (1993 - 2019).

Figure 12 shows the power spectrum of the Indian ocean at the same latitude. The annual, semi-annual, and tri-annual cycles appears to contain the highest peaks in the power spectrum, minus the peak at around 320 days. The semi-annual cycle (green vertical line) appears almost the same magnitude as the surrounding peaks from 170 - 190 days, where in figure 11, the semi-annual peak showed a higher peak. The smaller peak in the semi-annual cycle for the Indian ocean compared to

the Atlantic ocean may be due to the cross equatorial winds that reverse direction in summer and winter as a response from monsoon circulation [24].

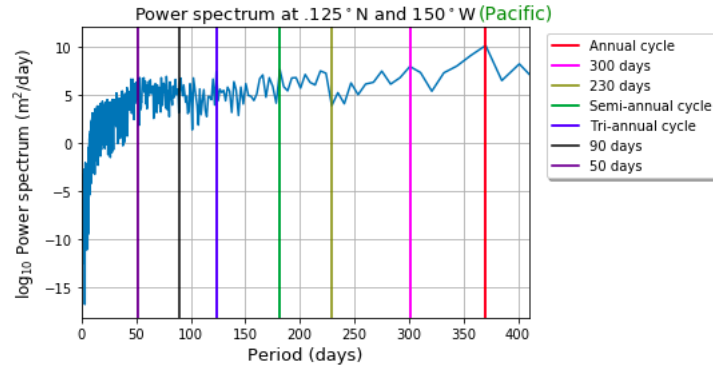


Figure 13: Power spectrum of Pacific Ocean time series (1993 - 2019)

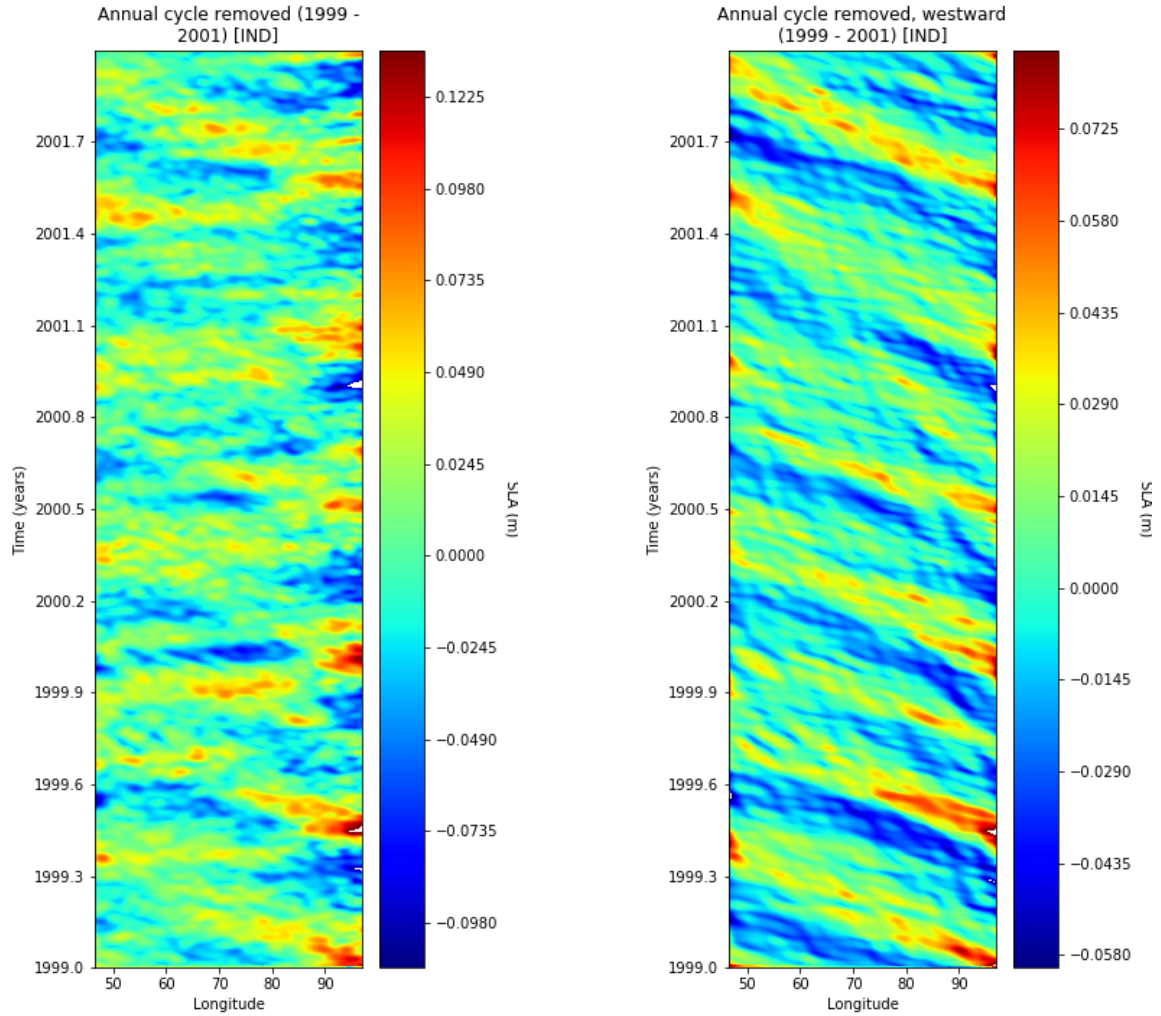
Figure 13 shows the period and power spectrum for the Pacific ocean at the same spatial location over the same range of years. The annual cycle dominates once again, with the semi-annual and tri-annual following suit. However, there is a smaller peak at 300 days, similar in magnitude of the power spectrum to the semi-annual cycle. For all the oceanic regions, the three main peaks in the power spectrum consist of the annual, semi, and tri-annual cycle. The significance of determining frequencies in the signal is to see what frequencies correspond to peaks in the power spectrum. It can also be seen that at all high frequencies (shorter periods), there is much less contribution to the power spectrum, but higher frequencies may still be of importance, especially when looking at higher-frequency gravity and mixed Rossby-gravity waves (assuming the classical, β -plane approximation). Lower frequencies give way to Rossby wave propagation indicating that Rossby waves may propagate on annual, semi, or even tri-annual cycle periods.

4.2 2D Fourier Transform and Phase speeds

Since the annual, semi, and tri-annual cycles were the three frequencies that resulted in the highest spectral peaks of the power spectrum, these signals were both isolated and/or removed leaving the remaining frequency band. For example, the annual cycle was removed, leaving all the other frequencies present. Then frequency bands were taken in twenty day intervals from 70 - 90, 50 - 70, 40 - 60, and 25 - 40 days. For each frequency band, the 2D Fourier transform was taken to isolate both the eastward and westward signals. The Radon transform was computed to determine the phase speed, which will later be compared to the theoretical models. The data segments for each ocean were split up into increments of 3 years. This was partially done for visualization purposes as a smaller time range allows for a better view into the nuances of the longitude-time plots but also the running time for Python was a lot faster when taking smaller chunks of the SLA data.

4.3 Classical Rossby waves

The first wave type that was found was the first mode Rossby wave in the Indian ocean from year 1999 - 2001 with only the annual cycle attenuated.



(a) Hovmoller plot showing the annual cycle removed from 1999 - 2001 in the Indian ocean

(b) Westward filtered Hovmoller plot (1999 - 2001).

Figure 14: Unfiltered and westward filtered Hovmoller plot over the Indian ocean (1999 - 2001) with the annual cycle removed.

Figure 14a shows the unfiltered signal with longitude on the x-axis and time on the y-axis. At first glance waves appear to be mainly zonally propagating eastward (positive slope) waves, particularly from decimal year 2000.8 - 2001.1, but there also appear to be traces of westward ones (negative slope) particularly in year 1999 - 1999.3 and 2001.5 - 2001.7. Around 90 degrees in longitude, there appears to be an intensification in the SLA magnitudes. This is most likely due to the presence of a mid-oceanic ridge known as the Ninety East ridge, which runs almost completely parallel through the 90th meridian at the center of Eastern hemisphere. It has an average width of 200 km and a maximum height of 3.5 km above the surrounding ocean floor of ≈ 4 km depth [25].

Figure 14b shows the westward filtered signal. The negative slopes are isolated from the original,

unfiltered Hovmoller plot. In the year 2001.5 - 2002, there appears to be a negative slope that is most uniform in SLA magnitude in comparison to other years which show some breaks in color, particularly year 2001.1 - 2001.4. There also seems to be an intensification in SLA amplitude, even before the crossing of the Ninety east ridge, at longitude 75° from year 1999.3 - 1999.6.

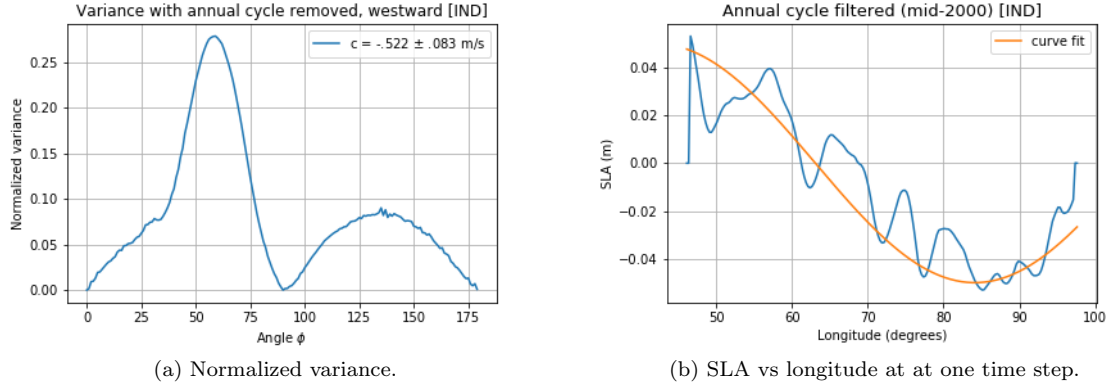


Figure 15: Figures showing first the normalized variance from the Radon transform and the SLA vs longitude to obtain the zonal wavelength.

Figure 15a shows the variance of the Radon transformed signal, with angle in degrees on the x-axis ranging from $0 - 180^\circ$ and the normalized variance on the y-axis. There is a peak in the variance at 52° , which corresponds to a phase speed of $-.522 \pm .083$ m/s, the negative sign indicating westward propagation (see appendix C for more details on determining the speed). There is a small rise in variance from $100 - 175^\circ$, which indicates that there may be some hints of eastward propagation in the slopes, as anything greater than 90° indicates eastward wave propagation. As the normalization factor (see appendix C) takes into account the different lengths that arise when rotating the Hovmoller diagram over a range of angles, the normalized variance must be picking up some subtleties which differ from the average inclination of the majority of the westward slopes. When looking at the non-normalized variance, the smaller peaks are much more reduced than others but the non-normalized variance does not take into account the differing lengths that arise from rotation.

In order to match the observational phase speed with the theoretical, classical model and determine if this may be a particular wave, the zonal wavelength must be determined. Figure 15b shows the SLA vs longitude averaged over all the latitudes ($\pm 2^\circ$) at one time stamp (mid-2000). A curve fit was also placed to get a better sense of the sinusoidal motion. There appears to be one wavelength that is about 1.5 times the extent of the Indian ocean, as there is not a complete cycle within the SLA vs longitude. When matching with the classical phase speeds for the different types of waves, the mode 1 Rossby wave from the classical model, assumes a zonal wavelength of 1.5 times the extent of the Indian ocean, outputs a wave speed of $-.561$ m/s. The wave speed obtained from the observational data is an under-estimate of the theoretical model. This may be due to the presence of the eastward zonal jet, an EUC known as the Wyrтки jet which is described as a semi-annual, wind forced zonal current along the central and eastern Indian ocean. The Wyrтки jet reaches $80 - 100$ m in depth from the surface of the ocean [26]. As the semi-annual cycle is the second most prominent frequency, once the annual cycle is removed, the eastward moving jet may be hindering westward wave propagation, potentially explaining for the over-estimation from the classical model.

In order to obtain the phase speed from the non-traditional model, the meridional decay scale must be looked into. Recall from the non-traditional approach that there is a dependency on the vertical direction, which does not allow for limits to be taken with the non-traditional approach to return to the traditional dispersion relation. This signifies that it is difficult to obtain a sense of what "type" of non-traditional wave, for example, non-traditional Kelvin/Rossby/gravity wave, etc. However the meridional structure can be investigated by extending the latitudinal region of the Indian ocean from year 1999 - 2001 from $\pm 2^\circ$ to $\pm 15^\circ$. This is to get a bigger picture of how sea level anomalies may change in the meridional (latitudinal) direction:

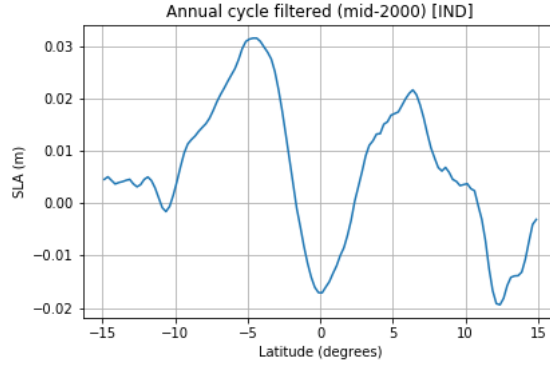
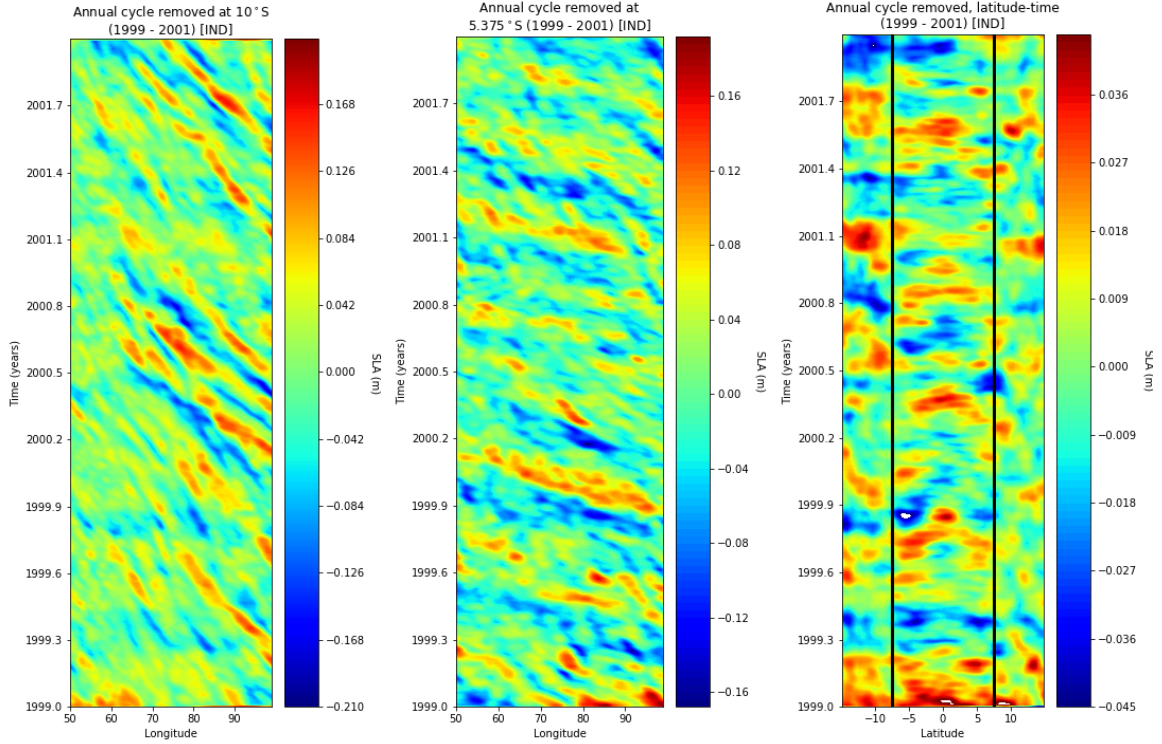


Figure 16: SLA vs latitude plotted to obtain the meridional structure.

Figure 16 shows the SLA vs latitude, with the annual cycle removed, averaged over all the longitudes for one time stamp (mid-2000, the same date for the zonal wavelength as in figure 15b). There appears to be a large dip in sea level anomaly amplitude at the latitudes close to the equatorial region, approximately $\pm 5^\circ$. There appears to be some sinusoidal patterns, particularly between $\pm 10^\circ$, but amplitudes decrease greatly south of 10° and increase slightly north of 10° . Sinusoidal latitudinal behavior is not necessarily expected as the separation ansatz for the non-traditional approach assumed for a positive l , a Gaussian type of meridional decay supplemented by Hermite functions having a number of nodes determined by n .

Assuming a meridional decay scale of 1110 km, extending $\pm 5^\circ$ in latitude, and the zonal wavelength of 9990 km obtained from figure 15b, the non-traditional phase speed obtained from equation (79), gives a high phase speed of 20.19 m/s for mode $n = 1$. However, the waves for the non-traditional model were for a non-two layer fluid, so perhaps this phase speed is comparable to barotropic waves. If the decay scale is smaller, anything less than 2° latitudinal extent, then the phase speeds align in magnitude with ones obtained from the variance of the Radon transform.



(a) Hovmoller plot showing the annual (b) Annual cycle removed from 1999 - (c) SLA vs latitude plot from 1999 - cycle removed from 1999 - 2001 in the Indian ocean at 5°S, show- 2001. Black lines indicating the struc- Indian ocean at 10°S. tural "core" of the equatorial boundary layer.

Figure 17: Directionally unfiltered Hovmoller plots at off-equatorial regions (10 and 5°S) and the latitude-time plot showing change in SLA magnitudes over latitude.

In order to get a sense of how the wave propagation direction may change on and off the equatorial boundary layer, figure 17a shows the longitude-time plot with the annual cycle removed (from years 1999-2001) at 10°S off the equator. Even though there is no directional filtering here, the westward wave propagation is evident by the negative slopes. Figure 17b shows the directionally-unfiltered longitude-time plot at 5°S, closer towards the equatorial boundary layer and the latitude where from figure 16, the SLA amplitude begins to decrease. Figure 16 shows that on the approach of 5°S, the SLA amplitude gets larger. At 5°S, the westward propagation slope is not as steep, implying that the waves are moving faster, but westward movement is still prominent.

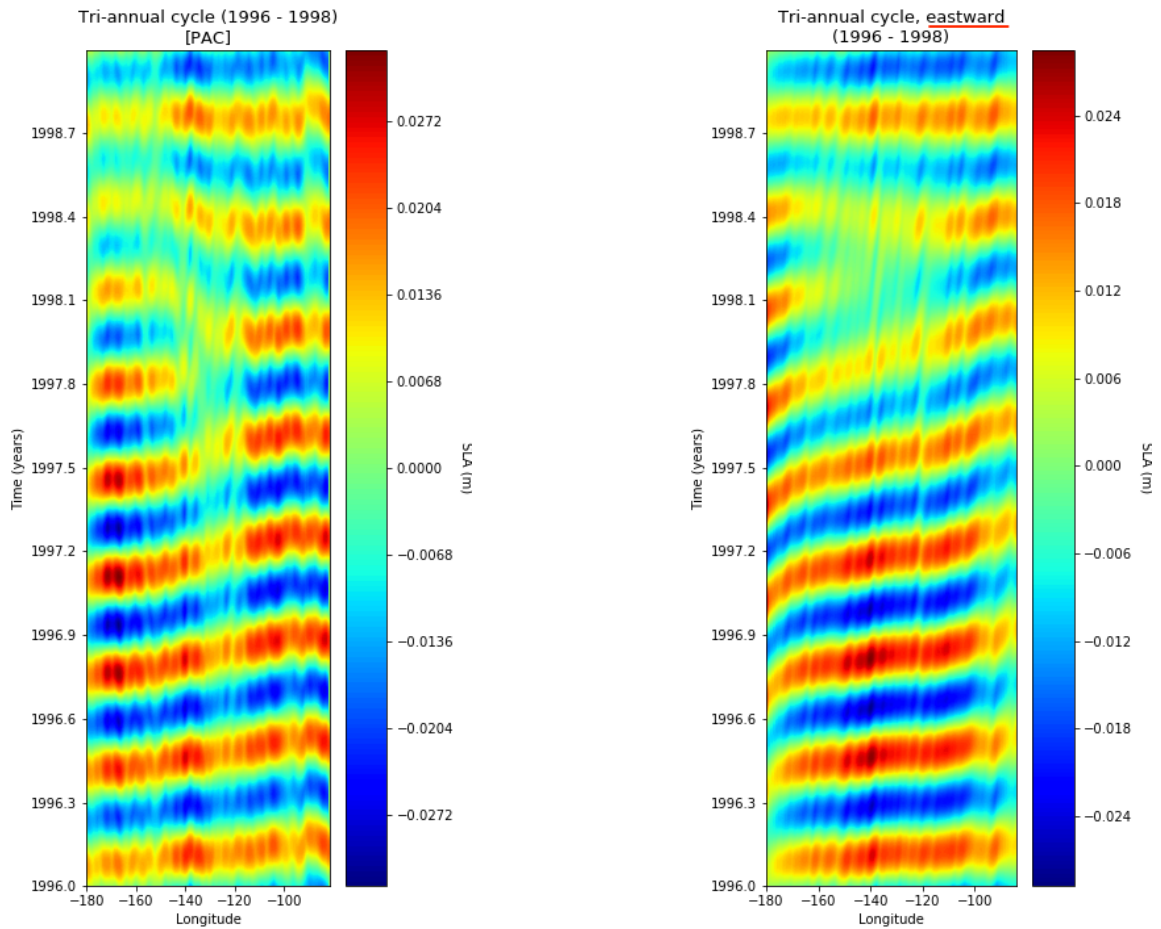
Figure 17c shows the *latitude*-time diagram to get a picture of wave propagation over the latitudinal extent ($\pm 15^\circ$). There appears to be a latitudinal "core", indicated between the black lines at $\pm 6^\circ$ in latitude. South of 5°S in figure 17c, some waves appear to be propagating towards the equatorial region. Within the equatorial region $< 5^\circ$ in latitude, meridional wave propagation is almost completely absent, particularly at the end of decimal year 2001.4, while south of 5°S there waves appear to have a negative slope, particularly at the end of year 1999 to the start of year 2000.

On five occasions the sea level anomaly shows a strong positive magnitude within the region indicated by the black lines, at time 1999, 1999.7, 2000.3, 2000.8, 2001.5. The SLAs also appear

to decrease in magnitude past 6°N . Figures 17a, 17b, and 17c show how there is a structural shift in the zonal propagation as one gets closer and closer to the equatorial region. Even though the equatorial boundary layer is typically defined as $\pm 2^{\circ}$ in latitude, there are already some meridional changes at $\pm 5^{\circ}$.

4.4 Classical Kelvin waves

There was detection of classical Kelvin waves within the tri-annual cycle in the equatorial Pacific ocean from years 1996 - 1998.



(a) Hovmoller plot showing isolated tri-annual cycle from 1996 - 1998.

(b) Eastward filtered.

Figure 18: Unfiltered and eastward filtered Hovmoller plot over the Pacific ocean (1996 - 1998) with only the tri-annual cycle isolated averaged over the $\pm 2^{\circ}$ latitudinal range.

Figure 18a shows the longitude-time diagram for the isolated tri-annual cycle frequency band. Even unfiltered, there is clear eastward propagation, with some small westward slope indications in

the beginning of year 1998. Figure 18b shows the diagram with the eastward filter applied. The slopes appear to be relatively uniform and oscillate between positive and negative SLAs from 1996 - 1997.5. At 105° in longitude, there appears to be a shift in SLA magnitude. This may be due to the presence of the East Pacific Rise which is a mid-oceanic ridge about 2.5 km in height relative to surrounding Pacific ocean depths of ≈ 5 km; the ridge is smaller in height than the Ninety East ridge in the eastern Indian ocean. It is called a "rise" because the slopes of the ridge are less steep [27]. Around year 1998 - 1998.5, there appears to be a break in the uniformity of the slopes, which may be explained by a strong positive el Nino anomaly. The east to west winds weaken over the Pacific, causing the thermocline to flatten, which results in masses of warm water to move towards South America, the eastern boundary of the Pacific [2]. Upwelling is reduced, which may cause a shutting down or reversal of zonal jets [28], which might explain for the change in slope and decrease in SLA magnitudes for that year.

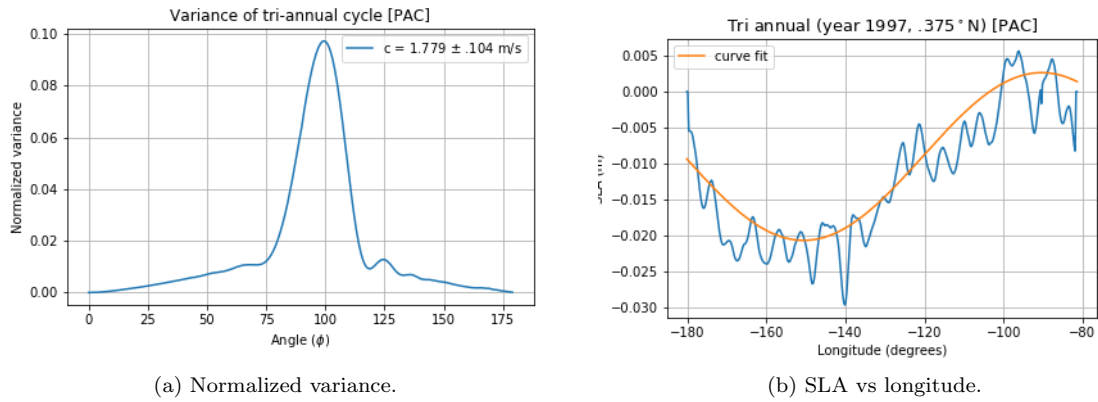


Figure 19: Figure 19a showing the normalized variance and figure 19b showing the zonal wavelength.

Figure 19a shows the normalized variance with a clear peak at 99°, which corresponds to a speed of 1.779 m/s. In order to compare to the classical, β -plane approximated model, the zonal wavelength was determined by plotting SLA vs longitude at one time stamp and latitudinal location, shown in figure 19b. There appears to be one wavelength within 1.5 times the size of the Pacific ocean basin, which gives a Kelvin wave speed of approximately 1.717 m/s, keeping in mind that this is very close to the assumed wave speed from the square root of the reduced gravity times the height of the mixed fluid column (1.7 m/s), as it should be since classical Kelvin waves are dispersionless. The classical model and observational wave speed are comparable to each other, except that the observational wave speed is higher than the model's speed output. However, this may be due to the eastward intensification of the zonal jets in the equatorial Pacific [29].

Similar to the Indian ocean, the SLA vs latitude is plotted to obtain a sense of the meridional structure over a larger latitudinal range ($\pm 15^\circ$).

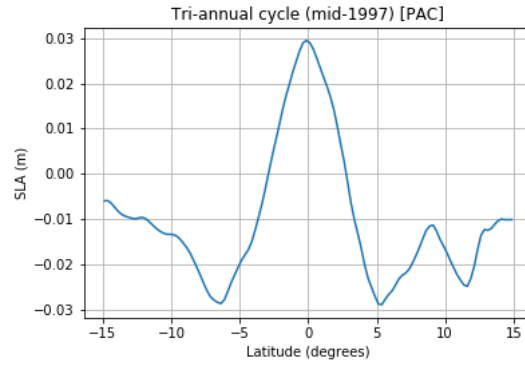
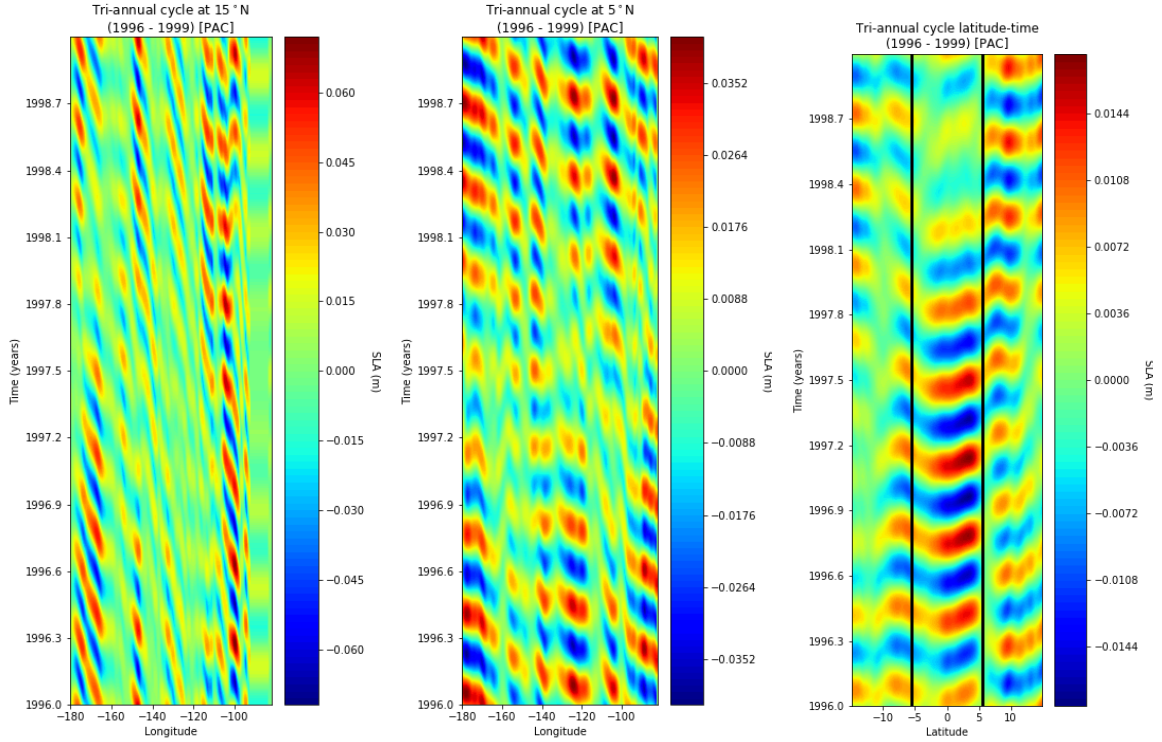


Figure 20: SLA vs latitude plotted showing meridional structure of the tri-annual cycle in the Pacific ocean.

Figure 20 shows the SLA of the tri-annual cycle vs latitude averaged over longitude in the Pacific. There appears to be a large increase in SLA amplitude starting at 6°S and ending at 5°N , corresponding to a change in SLA amplitude at similar latitudes to figure 16 for the Indian ocean. The sinusoidal shape is not as evident as with the zonal wavelength (SLA vs longitude) in figure 19b, but there is a sense of a Gaussian shape. The change in SLA amplitude towards the equatorial boundary layer is evident in comparison to off-equatorial regions ($\pm 10^{\circ}$), where there are smaller SLA magnitudes.

The same plot for the semi-annual cycle (not shown) showing the SLA vs latitude showed both a peak and trough within $\pm 10^{\circ}$ instead of just one defined peak at 0° with smaller, preceding amplitudes as seen for the tri-annual cycle (figure 19b).



(a) Hovmöller plot (1996 - 1999) of the (b) At 5°S, showing westward propa- (c) Directionally unfiltered, latitude-
tri-annual cycle isolated in the Pacific gation is less prominent. time plot.
ocean at 15°S.

Figure 21: Directionally unfiltered Hovmöller plots at off-equatorial regions (15 and 5°S).

Figure 21a shows the longitude-time plot with the tri-annual cycle isolated at 15°N. There are strong features displaying westward propagation off the equator. The presence of the East Pacific Rise at 105° in longitude is evident as there is a significant decrease in SLA magnitude at around 100°W. Figure 21b shows the Hovmöller diagram closer to the equatorial boundary region at 5°N, where the westward propagating slopes decrease in inclination implying faster wave speeds. There is a significant contrast between off and on equatorial regions as in figure 18a, where the directionally-unfiltered tri-annual cycle Hovmöller plot is averaged over $\pm 2^\circ$ showing primarily eastward propagating wave signatures.

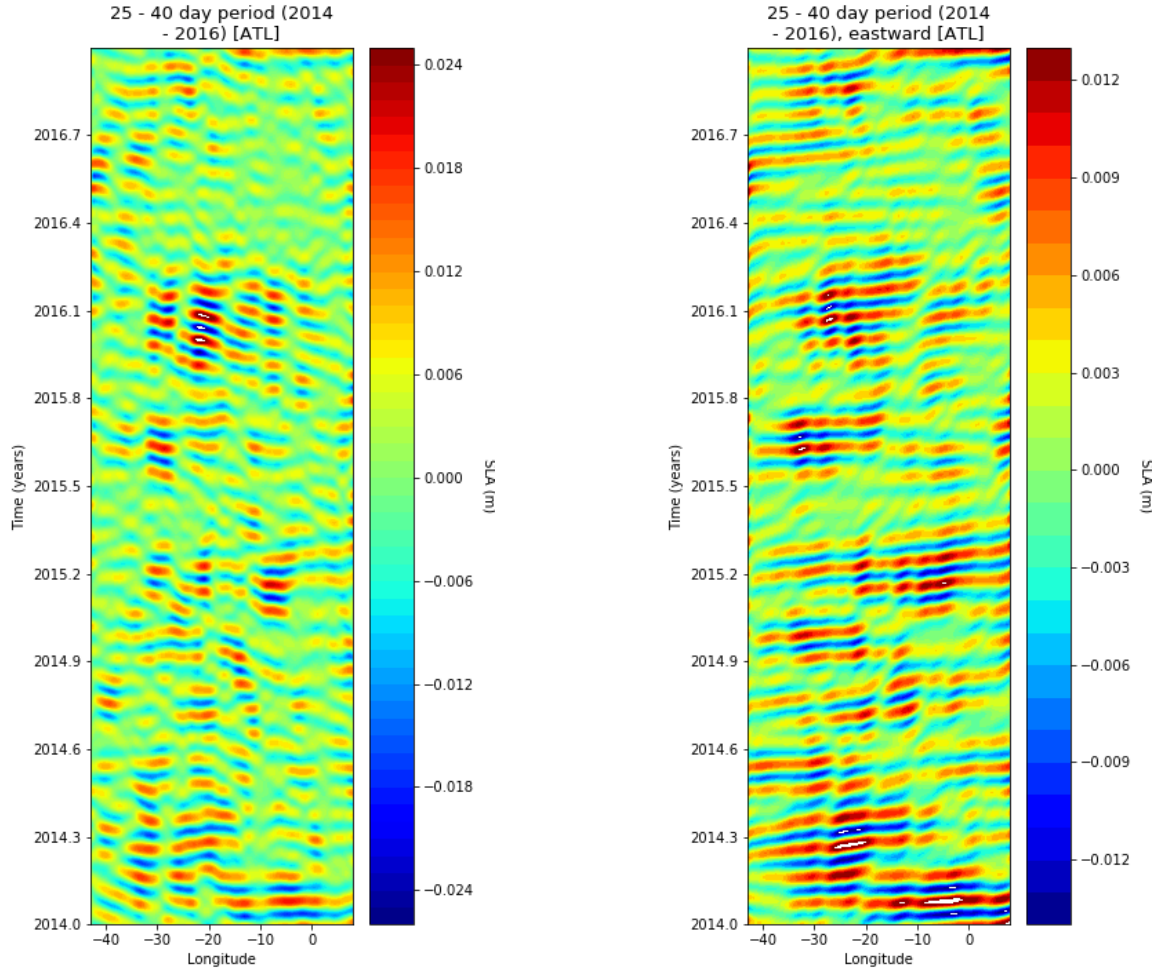
Figure 21c shows the latitude-time plot for the isolated tri-annual cycle. The vertical black lines indicate where the structure of the "core" occurs, the core being defined as the latitudes that transition between the large increase in SLA amplitude. There also appears to be a relatively constant fluctuation between positive and negative SLA values every third of a year, which is reasonable to be expected as the tri-annual cycle is isolated. The positive and negative anomalies decrease in the beginning of 1998, which was the year of a large ENSO event. Equatorial Kelvin waves are prominent at low frequency, intraseasonal time scales like the tri-annual cycle (120 day period). Kelvin waves are speculated to be forced by westerly wind bursts including the Madden-Julian oscillation (MJO) [30]. The MJO occurs in the troposphere and can be described as an eastward moving disturbance of rainfall, pressure, and wind fluctuations that occurs monthly or bi-monthly [31]. A

group of researchers demonstrated that there is not a statistically significant relationship between ENSO and the MJO due to nonlinearities [32], but there are suggestions that during the maxima of an ENSO event, the MJO weakens significantly or even becomes absent, which may result in a lack of equatorial Kelvin wave activity. The MJO time scale is monthly/bi-monthly and the period of focus in our case is 120 days, there were several studies showing that there were continuous westerly wind events (WWEs) between December 1996 and March 1997, followed by weaker easterly winds [15]. The presence of weaker easterly winds resulted in downwelling 120-day period Kelvin waves. The downwelling Kelvin waves may have resulted in shoaling of the thermocline which caused a reduction in the amplitude of eastward moving waves [15]. The combination between the weakening of the MJO and the increase in downwelling Kelvin waves from stronger WWEs may explain for the for the decreased SLA amplitudes in both figure 18b and figure 21c from the year 1998.

South of 5°S, the SLA magnitudes are not as prominent in amplitude differences in comparison to SLAs north of 5°N. Similar to the Indian ocean, off equatorial regions show primarily westward wave propagation. However, within the equatorial region, at the tri-annual cycle, the Pacific ocean shows mainly eastward propagation, while the Indian ocean in figure 14a, showed hints of westward propagating waves.

4.5 Classical Gravity waves

Gravity waves were potentially found in the Atlantic ocean (2014 - 2016). Gravity waves propagate at higher frequencies, but this gravity wave may be on the lower end of the high frequency spectrum, as the selected period band was 25 - 40 days. Gravity waves are known to propagate both westward and eastward. In this case, eastward waves are of focus.

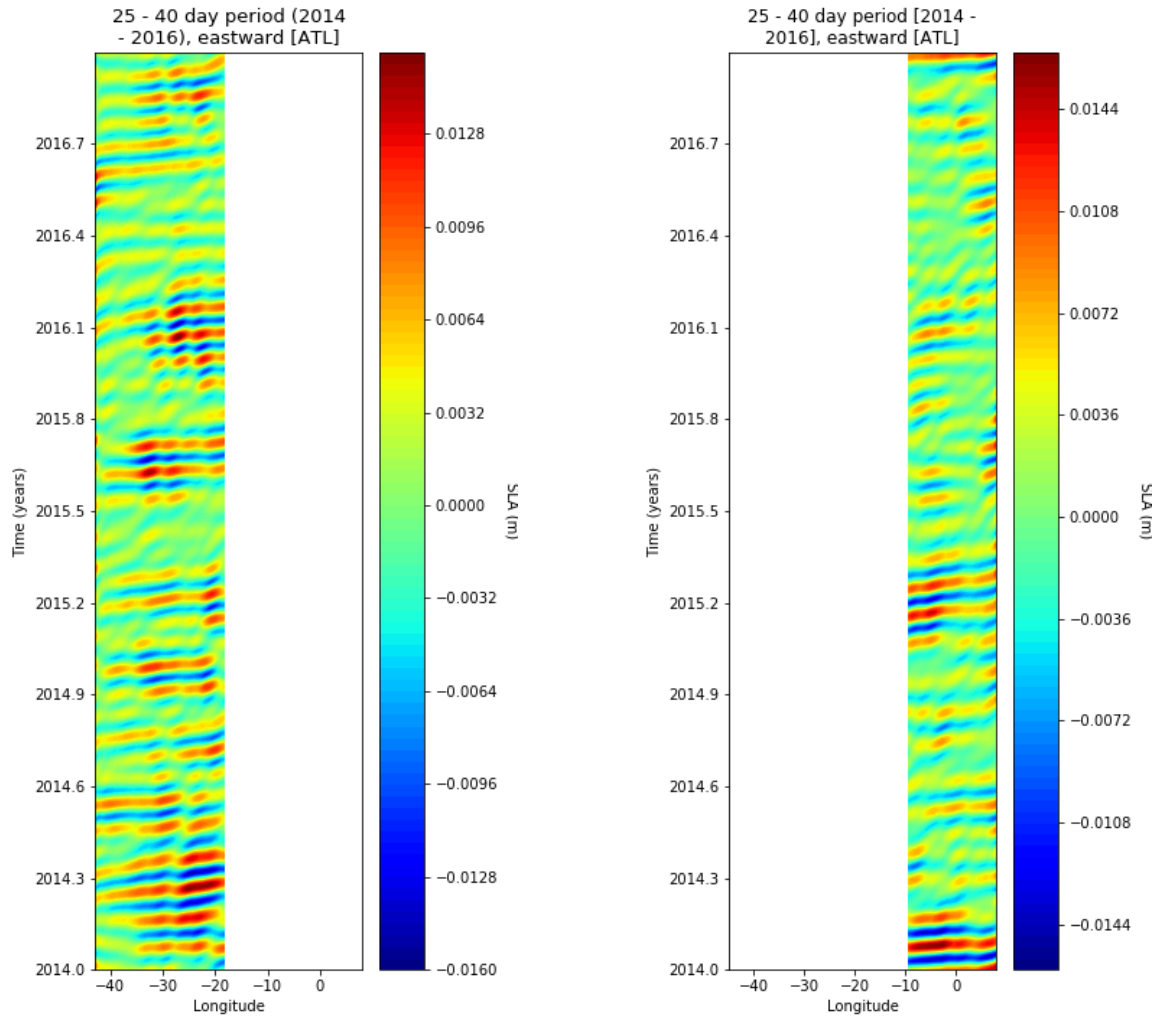


(a) Hovmoller plot showing 25 - 40 day period band from 2014 - 2016

(b) Eastward filtered.

Figure 22: Unfiltered and eastward filtered Hovmoller plot over the Atlantic ocean (2014 - 2016) over the period band of 25 - 40 days.

Figure 22a shows the unfiltered Hovmoller plot with in the 25 - 40 day period range. There does not appear to be a clear indication of eastward or westward prominence. Figure 22b shows the eastward filtered signal. The slopes are relatively even and uniform, particularly near year 2015.2. There are some regions where the SLA magnitude is intensified, for example earlier in the year 2014, 2015.2, and some patches in 2016. At 20°W, the mid-Atlantic ridge starts, which is one of the longest under water mountain ranges that extends almost to the opposite poles. It is about 3 km in height, relative to a depth of ≈ 4 km of the surrounding ocean, and 1000 km wide (or 9° in longitude) [33]. When taking the Radon transform and variance, the slopes of the signal need to be relatively equal in inclination or else there will be difficulty in determining a clear peak in the variance.

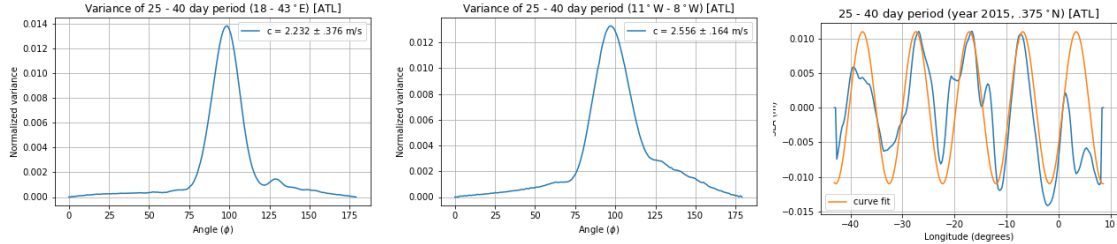


(a) 25 - 40 day period Hovmoller plot before mid-Atlantic ridge.

(b) 25 - 40 day period Hovmoller plot after the mid-Atlantic ridge.

Figure 23: Eastward filtered Hovmoller plots before and after the mid-Atlantic ridge.

Due to the presence of the mid-Atlantic ridge, figure 22b is split up into two segments, west and east of the mid-Atlantic ridge as shown in figures 23a and 23b. West of the mid-Atlantic ridge, there are more patches of positive and negative SLA values, while east of the mid-Atlantic ridge, there appear to be fewer.



(a) Variance west of the mid-Atlantic ridge. (b) Variance east of the mid-Atlantic ridge. (c) SLA vs longitude.

Figure 24: The first and second figure in the panel showing the variance to the west and east of the mid-Atlantic ridge. Then the figure showing the zonal wavelength.

Figure 23a shows the variance east the mid-Atlantic ridge, where the peak corresponds to a speed of 2.252 ± 0.376 m/s. Figure 23b is west of the mid-Atlantic ridge and corresponds to a speed of 2.556 ± 0.164 m/s. In order to determine the zonal wavelength, the SLA vs longitude was plotted for 2015 at 37.5° N in latitude in figure 24c. There are approximately 4 wavelengths in the entire Atlantic ocean basin signifying that one wavelength is equivalent to a quarter of the basin. Using the wavelength and wavenumber parameter, the classical eastward, high frequency gravity wave model suggests a wave speed of 2.748 m/s. It appears as if the classical model is slightly over-estimating the observed wave speed. This may be due to estimation of the wavenumber, as there may not be 4 complete wavelengths in the ocean basin, as the amplitudes in figure 24c do vary.

4.6 Classical Mixed Rossby-gravity waves

Taking the same frequency range but applying the westward filter may indicate the presence of westward propagating mixed Rossby-gravity waves. There was observational evidence using mooring and hydrographic measurements along the eastern equatorial Atlantic that gave indications of westward propagating, equatorially trapped Rossby-gravity waves from the paper "Equatorially trapped Rossby-gravity wave propagation in the Gulf of Guinea" [17]. The researchers took measurements in 4 different locations over a range of depths from 500 - 800 m. Keeping in mind that we are focusing on shallower, interfacial waves at depths between 100 - 200m, the depths they used are higher. Weisberg et al used a wavenumber analysis to obtain phase speeds from the observational data by separating zonal and vertical propagation to obtain a zonal phase speed of .45 m/s (in the range of .33 - .73 m/s), a zonal wavelength of 1220 km (880 - 1960 km), at a period of 30 days [17].

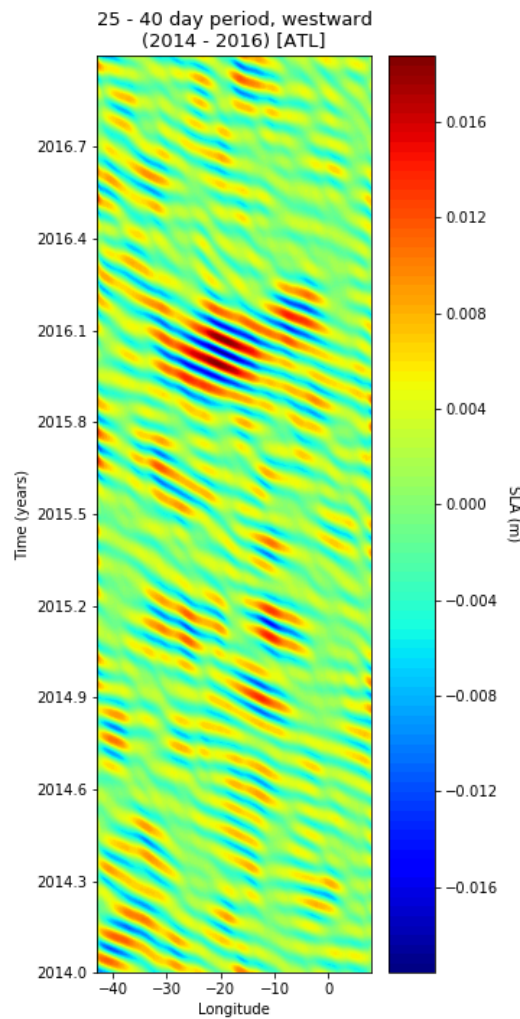


Figure 25: Westward filtered of 25 - 40 day period, 2014 - 2016 (Atlantic ocean).

Figure 25 shows the westward filtered Hovmöller diagram. The westward moving (indicated by negative slopes) have a higher inclination, which means that they move slower than eastward waves. There is a patch in early 2016 showing elevated SLA magnitudes. It is unclear as to why this might be, but other years are relatively uniform in sea level anomaly amplitude. There is a slight enhancement in SLAs between the 10 and 20°W region where the mid-Atlantic ridge is present, particularly for the beginning of 2015 and 2016.

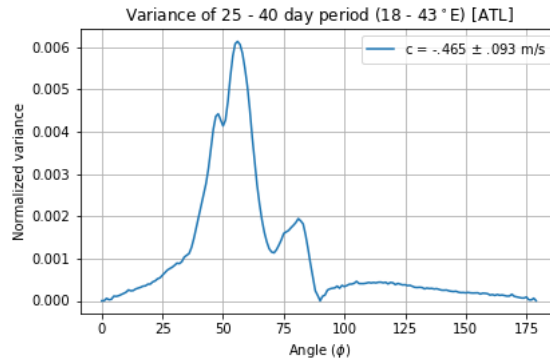


Figure 26: Variance of westward filtered equatorial waves in the Atlantic.

Figure 26 shows the variance of the Radon transform. The slopes of figure 25 are not at equal inclinations, as there is a peak occurring at 48°W , which corresponds with a speed of $.35\text{ m/s}$. However, the maximum peak gives a phase speed of $.465 \pm .093\text{ m/s}$. The speed found from Weisberg's observational study is comparable to the value found from the variance, as Weisberg's value falls within the uncertainty range. Weisberg isolated a period of 30 days, while our range includes 25 - 40 days. They estimated a zonal wavelength of 1220 km, while the wavelength observed is approximately 1400 km. Given these similar parameters from Weisberg's study to the altimetry observations, this motivates the presence of mixed Rossby-gravity waves. The presence of these particular waves may be related to the formation of equatorial zonal jets, as proposed by Fruman et al 2009 [35]. They argue that the MRG waves of short zonal wavelength and small to moderate amplitude are inherently unstable which may lead to the production of barotropic, zonally symmetric flow, in the form of zonal jets. Fruman et al simulated the production of short zonal wavelength MRG waves that gave way to *westward* flow, but when the model reached equilibrium or the MRGs had higher zonal wave-numbers, there was indication of *eastward* moving jets [35]. One thing to note here is that Fruman et al focused on much larger depths than $\approx 150\text{ m}$, ranging from 500 - 4500 m. However, the evidence that points to mixed Rossby-gravity waves being present in the equatorial Atlantic may help explain the instabilities that enhance or enforce the zonal current propagation.

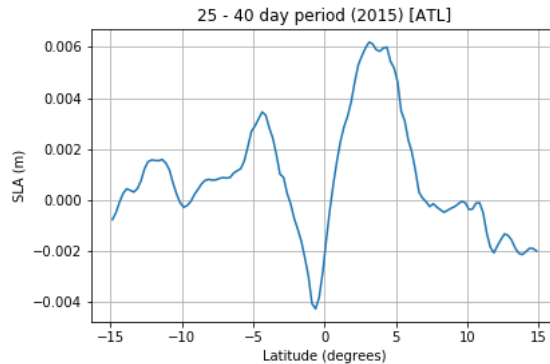
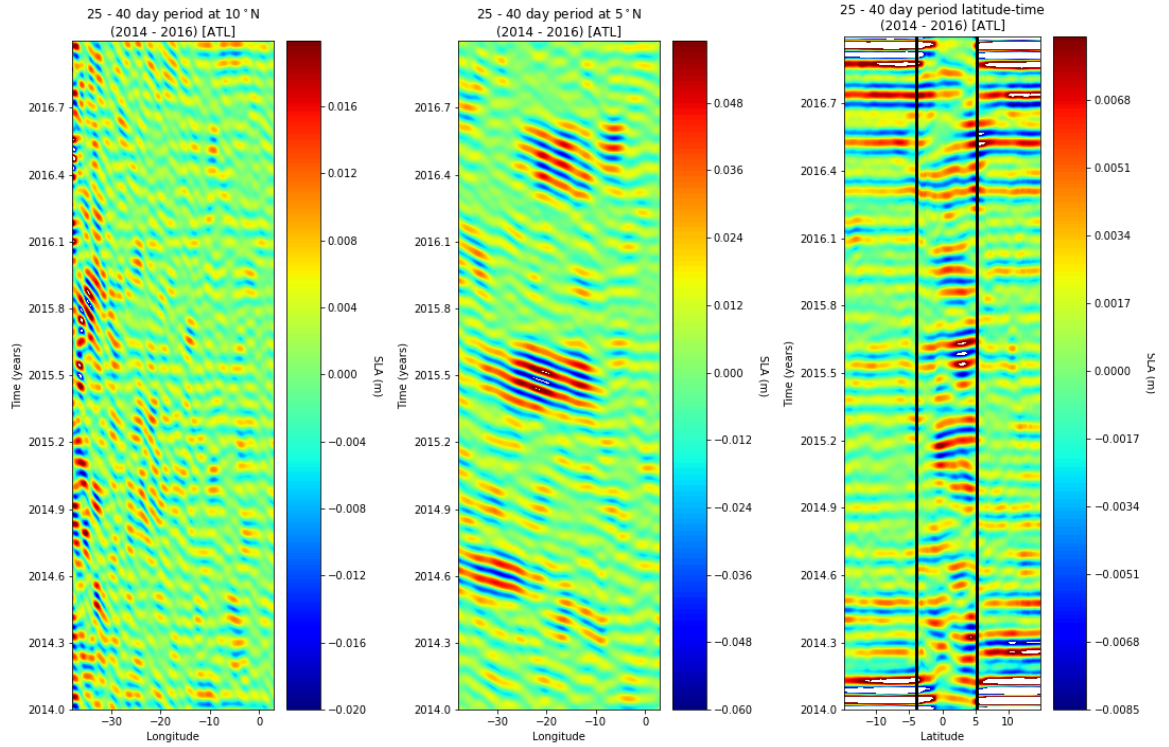


Figure 27: SLA vs latitude plotted showing meridional structure of the 25 - 40 days period band in the Atlantic ocean.

Figure 27 shows the SLA vs latitude at the 25-40 day period band at the start of year 2015. Unlike the Indian and Pacific oceans, in the Atlantic ocean there appears to be a trough and a crest within the $\pm 5^\circ$ latitudinal region instead of just one peak as there is for the Pacific ocean in figure 20. It is apparent that the SLAs greatly change in magnitude within the equatorial boundary layer. The larger amplitudes within the equatorial region and smaller SLA amplitudes outside $\pm 5^\circ$ make it difficult to estimate a decay scale, however the decrease in SLA magnitude from 5° to 0° extends 5° or 555 km. The zonal wavelength is then a quarter of the Atlantic ocean basin, 1430 km, which in equation (79) gives a non-traditional, mode 1 phase speed of -1.41 m/s for westward moving waves and 1.83 for eastward moving. Looking at figure 26 which shows the westward filtered variance, the phase speed obtained from the Radon transform is about 1 m/s less than the non-traditional one. However, the non-traditional model was for a non-two layer fluid and the estimation of the zonal wavenumber may be slightly off, potentially explaining for the discrepancy between the non-traditional phase speed and the one determined from the variance.



(a) Hovmoller plot showing the 25 - 40 day period band isolated from 2014 - westward propagation is less prominent. (b) Hovmoller plot at 5° S, showing 2016 in the Atlantic ocean at 10° S. (c) Directionally unfiltered, latitude-time plot.

Figure 28: Directionally unfiltered Hovmoller plots at off-equatorial regions at 10° and 5° N, including the latitude-time plot.

Figure 28a shows the longitude-time plot of the 25 - 40 day period band at 10° N. There are higher SLA magnitudes at the western boundary, most likely due to western intensification [2]. There appear to be westward propagating signals, however they appear to be shorter and choppier

over the zonal extent. When looking at figure 28b, this is the longitude-time plot taken at 5°N. The inclinations appear more clearly westward and the lines of propagation are more coherent. Figure 28c shows the latitude-time diagram over $\pm 15^\circ$. It is averaged over the entire zonal extent (48°W to 3°E). There appear to be some high SLA magnitudes in the beginning of year 2014 and end of 2016 equatorward and poleward of $\pm 5^\circ$. However, in order to accentuate the SLAs of higher magnitudes they were masked out (in white) to reveal a trend of higher SLAs confined within the $\pm 5^\circ$ latitudinal band. This is similar to the tri-annual cycle for the Pacific ocean where within the range of the $\pm 5^\circ$, there were higher and lower SLA magnitudes.

4.7 Comparison Between LADCP Measurements taken at the Equatorial Atlantic

Rabitti 2016 took instantaneous velocity measurements for a region in the equatorial Atlantic in the Ceará basin. There were five moorings in total, but for three of the moorings, Long Ranger Acoustic Doppler Current Profilers (ADCPs) were mounted at 1000 m facing upwards [1]. The measurements were taken mid-December of 2007 to mid-June 2009, for approximately a year and a half.

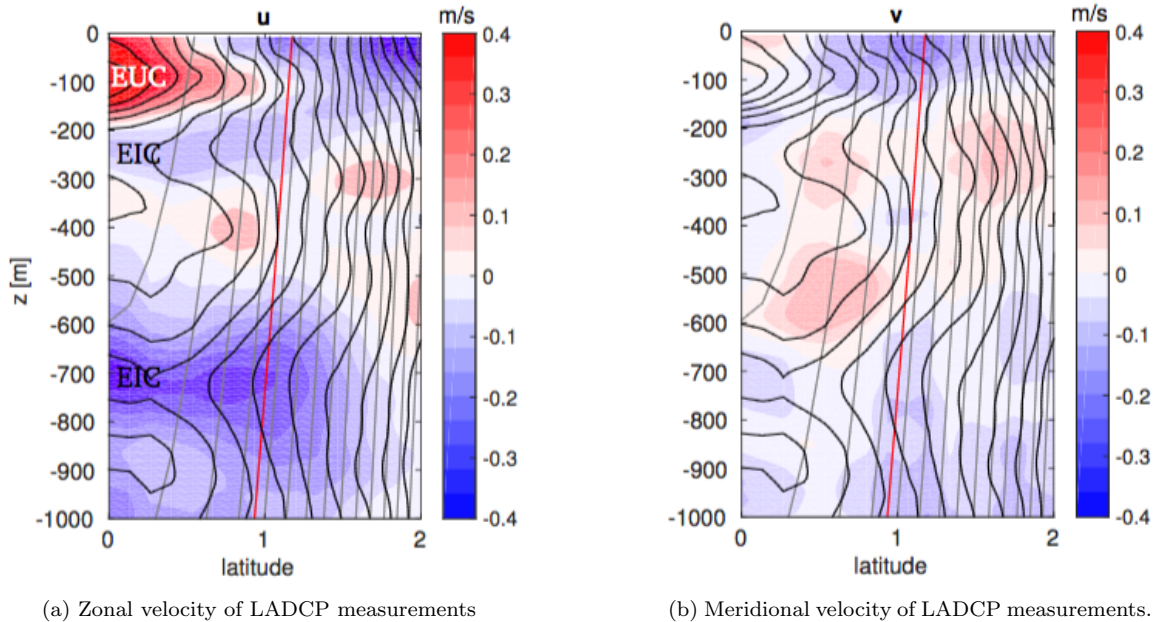
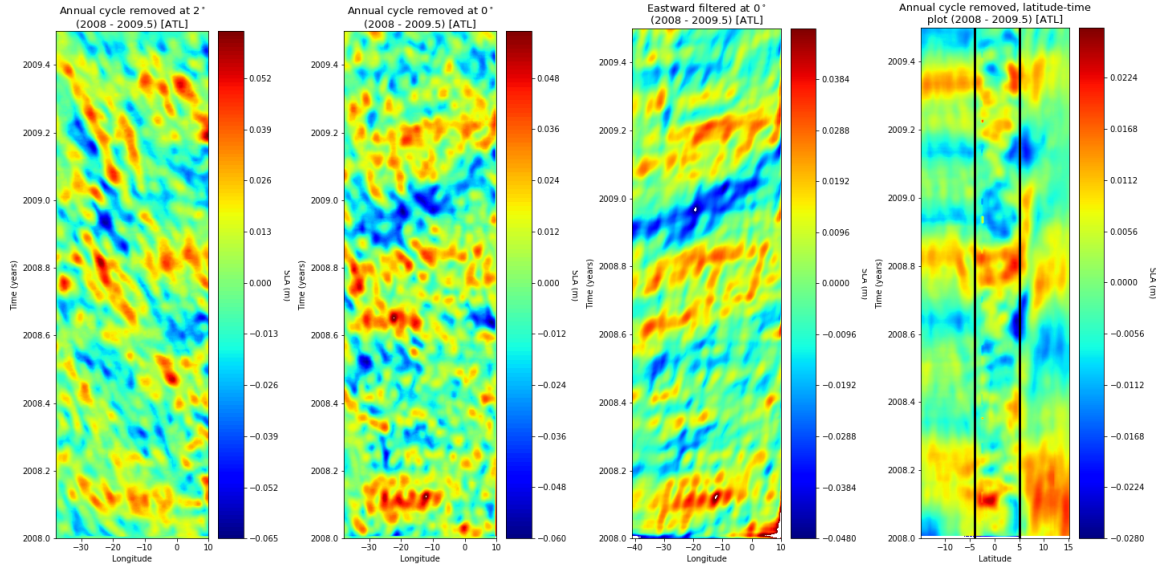


Figure 29: Figures showing the change zonal and meridional velocity with respect to the latitude from Rabitti 2016 [1].

Figures 29a and 29b show the zonal and meridional velocity changes with respect to latitude. The eastward moving equatorial undercurrent (EUC) within the first few hundred meters is present up until around 1° in latitude, then the zonal velocities become negative or westward moving. The EUC presents a peak velocity of 0.75 m/s within a 50-100 m depth, with mean velocity values at .43 m/s when averaged over the entire current area [1]. The meridional velocity in figure 29b is slower than the observed zonal speeds. There appear to be smaller vertical scales and more uniform behavior throughout the water column [1].

In order to investigate whether the satellite data may correspond to the trends shown in the LADCP data, a similar time period was taken of the Atlantic ocean sea level anomaly altimetry data from January of 2008 - July of 2009. The annual cycle is removed as it was the most dominant peak in the power spectrum. In Rabitti's observational data, the time variations of velocities are shown, implying that mean flows and speeds from waves of particular frequencies can be discriminated, which is also why all frequencies except the annual cycle were kept. Two latitudes were taken at 0° where the EUC is a maximum and eastward speeds were maximum, and 2° where westward zonal speeds are dominant.



(a) Hovmoller plot (2008 - 2009.5) showing the annual cycle removed at 2° . (b) Hovmoller at 0° . (c) Eastward filtered at 0° . (d) Latitude time plot.

Figure 30: Directionally unfiltered Hovmoller plots at 0 and 2° . Then the eastward filter applied and a latitude-time plot.

Figure 30a shows the primarily westward propagation from the negative SLA slopes at 2° . Then at 0° in figure 30b, the wave propagation appears to be eastward with the slopes less inclined suggesting faster moving waves. A directional, eastward filter is applied at the same latitudinal point of 0° as shown in figure 30c. It is evident that eastward propagation is dominant as the SLA amplitudes with the eastward filter applied is comparable to the directionally-unfiltered amplitude. Interestingly enough, when the Radon transform is applied to figure 30c and then the variance is taken, the phase speed is $.859 \pm .188$ m/s. The peak velocity found from the LADCP measurements taken at the level where the EUC is a maximum, was found to be .75 m/s [1], which falls within the uncertainty range of the eastward propagating phase speed from the variance. However, the main difference between the LADCP measurements from Rabitti et al's observations and the altimetry data used here is that the longitudinal extent is much greater than the LADCP measurements which measured the velocity at specific longitudes. Also Rabitti et al's observations showed time variations of velocities, discriminating waves at particular frequencies. This difference may explain

for the higher eastward phase speed found.

Figure 30d shows the latitude-time plot after being averaged over the entire range of longitudes. The first thing to notice is that the sea level anomaly amplitudes are much lower than the zonally propagating SLAs from figure 30b, where compared to the meridional LADCP measurements (figure 29b), the meridional velocity magnitude was much smaller in comparison to the EUC speeds. The black vertical lines show where the latitudinal structure appears to change when approaching the equatorial boundary layer.

5 Discussion and Conclusions

In this thesis, the traditional, β -plane approximation to model equatorial wave dynamics was compared to the non-traditional approach (developed by Maas 2007 [9] and Anna Rabitti's doctoral thesis on equatorial waves [1]). The dispersion relations between the two approaches vary greatly, as there is a vertical dependency for all the velocity components in the non-traditional method. One of the main differences between the mid-latitudes and the equatorial region is the presence of zonal jets, particularly the eastward moving equatorial undercurrent. There lies another difference in the equatorial region given the geometric shape of the earth and the changing height of the water column: there may be the presence of eastward propagating planetary Rossby waves due to PV arguments based on topographic Rossby waves. Observational sea level altimetry data were used to learn about the mechanisms and wave propagation that may result in or explain the eastward moving Equatorial Under Current, and to see if there may be the presence of these non-traditional types of Rossby waves.

The SLA data was converted to longitude-time plots and then a directional filter separating eastward from westward signals was implemented. A 1D spectral analysis was also used to determine the dominating frequencies of the signal and isolate specific frequencies. For all oceanic regions, the observational data shows that the changes in meridional and zonal currents, whether it be in direction or speed, occur within or close to the defined equatorial boundary layer. These changes include the shift from westward wave propagation in off-equatorial regions to strong eastward propagation within the equatorial belt.

Specific wave types that corresponded with the classical waves were found by obtaining the phase speed using the Radon transform to determine phase speeds more efficiently and accurately than determining the phase speed by manually computing the slopes of the Hovmoller plots. The directional filter and Radon transform have been used in the past to look for Rossby waves in the off-equatorial Indian ocean [40], however these two methods have never been used to look at the equatorial zone, focusing primarily on eastward wave propagation. The annual, semi, and tri-annual cycles were found to be the three most dominant frequencies for each of the ocean basins: Atlantic, Indian, and Pacific.

Phase speed propagation for higher frequency bands (15 - 60 day period range) in the Pacific ocean was almost 1 m/s higher than for the Atlantic and Indian ocean. The eastward moving wave phase speed for the annual cycle frequency isolated was 3.5 times higher in the Pacific than in the other two ocean basins. This increased eastward phase speed at the annual cycle may be due to the upwelling annual cycle (driven by Ekman and wave upwelling), where subsurface water is pumped upwards and forms a strip of tongue-like, cold water along the central and eastern equatorial Pacific which occurs at the start/end of the year [34]. The meridional structure (SLA vs latitude) of all the oceanic basins was relatively similar, showing either a peak or dip in sea level anomaly amplitude within $\pm 5^\circ$ in latitude. The peak/dip corresponds to the seasonal variation of the SLAs, as a peak mainly corresponded to summer months and a dip was consistent with winter months.

Presence of a mode 1 Rossby wave was found in the equatorial Indian ocean when removing the annual cycle and leaving the remaining frequencies. A Kelvin wave was found in the equatorial Pacific at a period of 120 days (tri-annual cycle). An eastward gravity and westward mixed Rossby-gravity wave were found at a 25 - 40 day period in the Atlantic ocean. It was also observed that within the equatorial region, with the tri-annual cycle isolated only, the Pacific ocean primarily showed eastward propagation, while the Indian ocean showed traces of westward moving waves. The Atlantic Ocean SLA altimetry Hovmoller plots with the annual cycle removed were comparable to the zonal velocity structure of Rabiti et al as there was primarily westward propagation off the equatorial boundary layer, and within the boundary layer there was mainly eastward propagation. The maximum velocity of the EUC aligned with the phase speed determined from the eastward filtered Hovmoller plot along the equator at 0° .

5.1 Limitations and future work

The limitation of some of the methods lies in obtaining the observational phase speed using the Radon transform. Overall, the directional filter works well in isolating eastward or westward only features, and the Radon transform obtains phase speeds when the slopes of the Hovmoller plot are inclined evenly. However when the Hovmoller plot lines are inclined unevenly, the variance of the Radon transform may pick up other inclinations and there will not be a clear peak in the variance, as shown in figure 26, when obtaining the phase speed of the westward mixed Rossby-gravity wave. The degree resolution of the Radon transform could also be smaller (currently at 1°), which would improve the differences in phase speeds depending on the angle. For example, there is a phase speed difference of ≈ 1.5 m/s between an angle of 93° and 94° .

Overall, the phase speeds from the observations hold relatively well with the traditional β -plane approximated model, when matching the observational, zonal wavelength profile to the traditional dispersion relations to obtain model-based phase speeds. However there are some ambiguities when determining both the zonal wavelength and the meridional decay scale. When determining the zonal wavelength by plotting the SLA vs longitude, the curve fitting used to obtain the sinusoidal structure did not always align with fluctuations in the SLA amplitude. The SLA vs longitude provided a basic idea of the zonal wavelength, however it was based more on estimation from the curve fit, which often indicated that the wavelength exceeded the ocean basin to a certain extent. It is prudent to obtain a coherent picture of the zonal structure of the observational data in a more methodical way, which goes for obtaining the decay scale as well.

In all three ocean basins, there appeared to be strong variation in amplitude with the SLA vs latitude towards the equatorial region and smaller SLA fluctuations in off-equatorial regions. This is excluding the higher frequency band in the Atlantic where there were dominant SLA amplitudes outside the equatorial belt, which were masked out to obtain a better sense of the SLA magnitudes within the inner equatorial region. However, the smaller fluctuations in off equatorial regions for the rest of the frequency bandwidths created difficulties in pinpointing a meridional decay scale l as the amplitudes differed over the range of latitudes, which in turn made estimating non-traditional wave speeds difficult. The non-traditional wave speeds varied greatly in magnitude, depending on the choice of l . Smaller values given the extent of no greater than 2° in latitude gives phase speeds similar to those from the classical model, however there needs to be a more formulaic way of determining values for the meridional decay scale.

The mechanisms behind the eastward propagating zonal undercurrent still remain elusive. This is especially true for the Pacific ocean, as there is clear eastward, wave propagation throughout the whole range of the Pacific ocean, particularly at the tri-annual cycle. However there has been speculation that the destabilization from barotropic shear instability of shorter zonal wavelength,

longer period mixed Rossby-gravity waves may result in the formation of the zonal jets [35], where the observational data detected the presence of mixed Rossby-gravity waves in the Atlantic. There is a lot more to learn about the equatorial ocean, particularly in linking the non-traditional phase speeds with the observational ones by obtaining a more exact estimation of the meridional dependency. The elusive eastward propagating Rossby wave has yet to be found as well, but given that the directionally unfiltered Hovmoller diagrams showed primarily eastward propagation within the equatorial belt, and that eastward moving signals can be isolated, perhaps using those techniques for other types of data, for example sea surface temperature, may allude to the non-traditional eastward planetary Rossby wave.

Acknowledgement

I would like to express my gratitude for the many people who have helped me to shape this thesis, first of all Professor Leo Maas for his incredible insight and support. I really appreciated our weekly meetings to discuss the project. Due to the pandemic, the last few months called for an unprecedented time, also requiring adaptation to different work environments, but Leo's open communication was extremely helpful during this period of change. I would also like to express my appreciation to other members of IMAU. I am grateful to René van Westen for the Python discussions and for (hopefully) not minding my dropping by the office unexpectedly! Thank you to Daan Reijnders for inspiration on the spectral analysis of the satellite data. Thank you to Grant Francis for helping me debug Python programs and for being a great study buddy. Thank you to Irene Kruse and Evelyn Workman for all the good times in Utrecht outside of the coursework and thesis. Lastly, I am thankful to the Institute of Marine and Atmospheric research Utrecht (IMAU) for the wonderful scientific community and consistent support. I will cherish this experience in Utrecht forever!

6 Appendices

6.1 Appendix A: Spectral analysis: One-dimensional discrete Fourier transform

Before performing the 1D spectral analysis, a manual frequency array is constructed. The average sample time (in years) is determined by taking the time difference between each measurement. Then the number of samples per day (sample rate) is found by taking the inverse of the sample time and multiplying by 365 days. The Nyquist frequency, the maximum frequency of the signal, is determined by taking half the sample rate [36]. The frequency array for the entire time series goes from 0 to the Nyquist frequency in step sizes of Δf , which is the sample rate (per day) divided by the total number of sample points:

Average sample time	.0028 years
Sample rate	.9712 samples/day
Nyquist frequency	.4856 days ⁻¹

The discrete Fourier transform being defined as:

$$X_k = \sum_{n=0}^{N-1} x_n \cdot \exp\left(-\frac{2\pi i}{N} kn\right), \quad (97)$$

where n represents the discrete time, x_n is the value of the signal at the specified time index, k being the frequency array, and N is the total number of frequencies.

The explicit discrete Fourier transform is 1-dimensional multiplied by the sea level anomaly data (stored as a 3D matrix: time, latitude, longitude), so the phasor matrix (the complex exponential) is stored as a 2D array with dimensions of time and frequency, where each unique frequency and the corresponding time series is stored in the initialized array. The transformed signal outputs both a real and imaginary component. The amplitudes of the cosine waves are contained in the real part, and the sine wave amplitudes are in the imaginary part [36].

Parseval's theorem for the DFT shows the relationship between the power (variance) of the signal (the mean of the square of the detrended signal integrated over time) is equal to the frequency integrated power spectral density of the signal [37]:

$$\sum_{n=1}^N x(n)^2 = \frac{1}{N} \sum_{k=1}^{N-1} |C(k)|^2. \quad (98)$$

$x(n)$ is the standardized and tapered SLA time series, $C(k)^2$ is the power spectral density (the amplitudes in Fourier space squared and added together), and N is the total number of samples.

Parseval's theorem is useful as a means of checking the relationship between the spectral density in Fourier space to the square of the signal and to ensure that the constructed DFT is showing spatial results equivalent to the variance. After the power spectrum is computed by taking the absolute square of equation (97), the frequencies at which there are peaks in the power spectrum can be investigated, and thus the dominating signals driving the variations in sea level height can be determined.

Higher frequencies in the power spectrum can be high-pass filtered using a Butterworth frequency filter. The high pass filter passes the signal with a frequency higher than the cutoff frequency and attenuates the signal lower than that, which can be described as [36]:

$$R = \frac{1}{\sqrt{1 + \left(\frac{f}{f_c}\right)^{2n}}}, \quad (99)$$

where R is the transfer function of the filter, f is the frequencies of interest, f_c is the cutoff frequency, and n is the order of the filter [36]. The higher the order n is, the greater the roll off rate is between the frequency pass and cutoff band is.

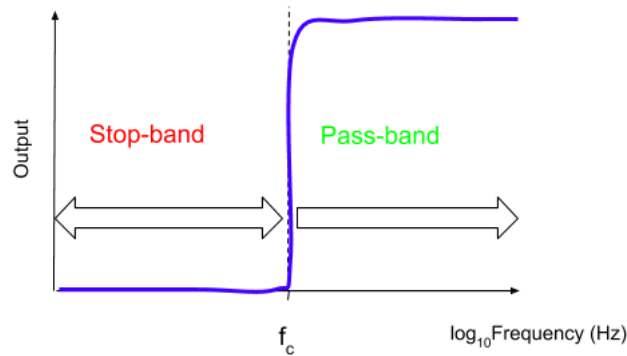


Figure 31: High pass Butterworth filter, where the order n will change the rolloff rate between the stop and pass-band.

6.2 Appendix B: Two-dimensional Fourier transform

The SLA altimetry data was converted into longitude-time (Hovmoller) plots. These types of diagrams are commonly used to plot atmospheric or oceanic data to highlight the role of wave propagation. The first observational evidence of planetary Rossby waves was found through longitude-time sections of filtered sea level data by Chelton et al 1996 [38].

The axes of Hovmoller plots typically consist of longitude on the x-axis and time on the y-axis, where the latitude can be averaged over a certain length or the latitude can be taken at just one point. For all cases of the equatorial Atlantic, Indian, and Pacific oceans, the latitudes were averaged over $\pm 2^\circ$. There have been a few studies that show westward-propagating Rossby waves can be seen more clearly from Hovmoller plots when a "westward-only" filter is applied [39], [40]. The westward only filter removes all stationary and eastward propagating signals by removing signals in the second and fourth quadrants of the frequency-wavenumber space, keeping only signals with a negative zonal wave number and positive frequency [41]. This idea of the filter can be applied to obtain eastward-only propagating signals as well, where the signals would be removed from the first and third quadrants in frequency-wavenumber space. Since there is theorized to be an eastward propagating, planetary Rossby wave in the equatorial zone, an eastward only filter will help to isolate solely eastward moving waves.

The discrete 2D Fourier transform for the longitude-time plots is:

$$F(u, v) = \frac{1}{XY} \sum_{y=0}^{Y-1} \sum_{x=0}^{X-1} f(x, y) \exp\left(-2\pi i\left(\frac{xu}{X} + \frac{yv}{Y}\right)\right), \quad (100)$$

where x and y represent the rows and columns of the 2D matrix, or in our case, longitude and time. For the latitudinally-averaged SLA data, the eastward and westward filter is taken by applying equation (100) to the data matrix.

In order to isolate eastward-only signals in 2D Fourier space, the frequency array was split in half, with the first half being set completely to zero. After half of the frequencies, denoted u were nullified, the zonal wave numbers v were split into two, and the second half of the wavenumbers were set to zero. This is equivalent to removing the first and third quadrants in frequency wavenumber space to remove all the westward propagating signals.

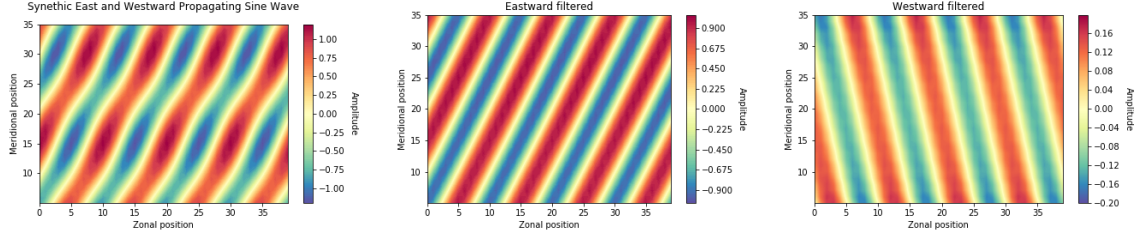
After the filter is applied by setting half of the frequency and wavenumbers to zero, depending on the desired eastward or westward direction, the inverse 2D FT needs to be taken to convert back into time-space from Fourier space:

$$f(x, y) = \sum_{u=0}^{X-1} \sum_{v=0}^{Y-1} F(u, v) \exp\left(2\pi i\left(\frac{ux}{X} + \frac{vy}{Y}\right)\right), \quad (101)$$

where $F(u, v)$ is the 2D spectrum of the original signal (longitude-time matrix). A quick example of the filter is applied to an eastward and westward propagating synthetic sine wave:

$$f(x, y) = \sin\left(\frac{\pi x}{5} - \frac{\pi y}{10}\right) + .2 \sin\left(\frac{\pi x}{5} + \frac{\pi y}{10}\right), \quad (102)$$

where x and y are the zonal and meridional dimensions. The eastward signal is the first and the westward component represents the second term with a smaller amplitude.



(a) Primarily eastward but also westward propagating signal. (b) Eastward filtered sine wave. (c) Westward filtered sine wave.

Figure 32: Original signal, eastward, and westward filter.

Figure 32a shows the combined eastward and westward propagating synthetic sine wave, but the eastward direction is more prominent due to the higher initial amplitude. Figure 32b and 32c show the eastward and westward filtered signals.

6.3 Appendix C: Radon transform

The filtering process now enables the Radon transform to be implemented, which is a method used to obtain phase speed properties from Hovmoller diagrams. The Radon transform of a 2D function, in our case the longitude-time plots, works to describe the intensity of an image by computing the integral of the function at an arbitrary line s , which is inclined at a specific angle from the x-axis (longitude) [42]. It is the projection of the image intensity along a direction normal to the angle ϕ , where s is the projected coordinate.

For a range of angles, the variance of the Radon transform is taken, and where the projection axis s is exactly perpendicular to the Hovmoller plot lines (whether it be westward or eastward propagating lines), that is where the variance of the RT is at a maximum. The angle can thus be determined, and through a series of trigonometric computations, the phase speed can be found [40].

The discrete Radon transform of a 2D function $f(x,y)$ is rotated over a range of angles of ϕ ($0 \leq \phi < 180^\circ$) and summed is defined as:

$$g(\phi, s) = \sum \sum f(x, y) \delta(x \cos \phi + y \sin \phi - s) dx dy, \quad (103)$$

where the δ function can convert the 2D summation into a single line integral (dl) along the line $s = x \cos \phi + y \sin \phi$ [43]:

$$g(\phi, s) = \sum f(s \cos \phi - l \sin \phi, s \sin \phi + l \cos \phi) dl. \quad (104)$$

$f(x, y)$ is the original 2D function, which is then converted into the the projected coordinate (s) through trigonometric functions.

After the Radon transform is taken, it must be normalized. The Radon Transform can be normalized by dividing the RT of the Hovmoller (of a specific length (l, t)) by the RT of the RT matrix composed solely of ones but with the same dimensions of the original image. The RT of the matrix with ones is divided by the RT of the original signal, Hovmoller plot (the signal not being comprised of ones). The Radon transformed data for both signals consists of a 2D array with values along the projected coordinate corresponding to the various angles ($0 - 180^\circ$):

$$\text{Normalization} = \frac{\text{RT of signal}}{\text{RT of empty array of ones}} = \frac{g(\phi, s)}{g_1(\phi, s)}. \quad (105)$$

After the Radon transform is taken, the variance can be taken by squaring the RT divided by the normalization and summing over the projected coordinate s to get one value per angle:

$$\text{Variance (RT Energy)} = \sum_{s=0}^{\infty} \left[\frac{g(\phi, s)}{g_1(\phi, s)} \right]^2 \quad (106)$$

where $g(\phi, s)$ is the discrete Radon transformed data and $g_1(\phi, s)$ is the normalization factor over a set of angles (0 to 180°).

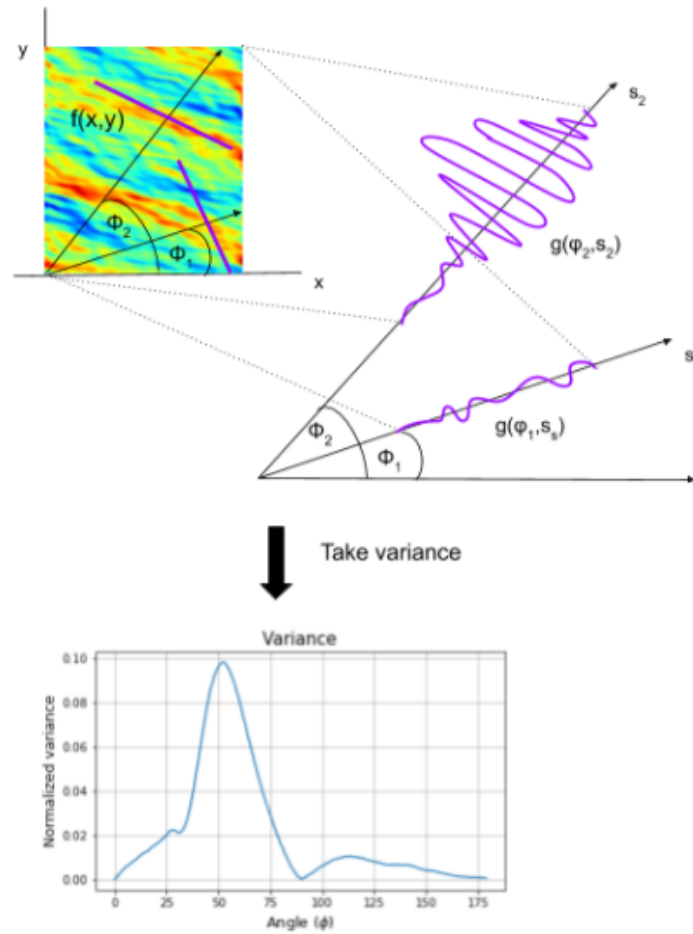


Figure 33: Scheme of the Radon transform and then the variance of the RT is taken.

Figure 33 shows the schematic visual of the Radon transform. Looking at the Hovmoller plot showing some westward propagating wave signals, the RT works by first integrating (or summing) over each of the purple lines for different angles, the perpendiculars of the rotated axis. The result of

adding over all the perpendiculars to the projected coordinate s , results in the 1D purple, squiggly lines ($g(\phi, s)$). The values of $g(\phi_1, s)$ along angle ϕ_1 corresponding to the Radon transformed purple line is smaller than those for ϕ_2 . This is because the SLAs perpendicular to the rotated axis for angle ϕ_1 consists of both positive and negative SLA values, to a certain extent, end up cancelling each other out when taking the sum. However for the diagonal at angle ϕ_2 , the perpendicular to the projected axis is uniform in magnitude, resulting in the sum being larger since there are minimal positive or negative anomaly values canceling with each other. This is why the summation for ϕ_2 is larger, as the the purple squiggly line has a larger magnitude than at ϕ_1 .

In order to create the angle rotation of the image, Python's `Scipy ndimage` function rotates the image by increments of 1° . As the image is rotated, the diagonal that is formed from the tilt of the angle ϕ from the x-axis is summed over the projected axis s , where the 2D image is converted into 1D. Each sum is saved in a unique spot for each differing angle. For each purple squiggly line, and depending on the angle, the size of the projection vector needs to be specified. As each image is rotated a certain angle, each projection that is saved in the projection vector has a differing length, which is accounted for by the normalization. The diagonal of the image is the maximum length that the purple projection line can possibly be.

The variance or energy of the RT from equation (106) is taken for each angle and then plotted. Where the variance is at a maximum, that is where the angle projected axis (s) is exactly perpendicular with the slope of Hovmoller plot lines. This angle can be converted to phase speed by taking the tangent and using the conversion [42]:

$$\text{Speed} = -\tan \phi \cdot \frac{\Delta x}{\Delta t} \cdot \frac{111000m \cos \phi}{86400s}, \quad (107)$$

where ϕ is the angle where the variance is at a maximum, Δx and Δy are the resolutions in longitude and time. For the SLA datasets, the resolution in longitude is $.25^\circ$ and the time resolution of when a measurement is taken is every 1.02 days. The last term is to convert the speed into meters/second.

6.3.1 Projection-slice theorem

The projection (or Fourier) slice theorem states that the Fourier transform of the 1D projection of a Radon transformed function will be equivalent to taking a 2D Fourier transform of the original function, and then slicing it through the origin, parallel to the projection line [40]:

$$F_1 P_1 = S_1 F_2, \quad (108)$$

where expressed in operator terms, F_1 and F_2 are the one and two-dimensional FT operators. P_1 is the projection operator (or RT), where the 2D function is projected into a 1D line. S_1 is then the slice operator which takes out a 1D central slice from the 2D FT of the original image [44]. This can also be re-written as:

$$F[g(\phi, s)] = F(u, v), \quad (109)$$

where F stands for the Fourier transforms, $g(\phi, s)$ is the RT, and $F(u, v)$ is the 2D Fourier transform of the 2D image.

The 1D Fourier transform in integral form of the RT (projection function) is given as:

$$G(\phi, \omega) = \int e^{-i\omega s} g(\phi, s) ds \quad (110)$$

where $g(\phi, s) = \iint f(x, y) \delta(x \sin \phi - y \cos \phi - s) dx dy$. With $g(\phi, s)$ plugged into equation (110):

$$G(\phi, \omega) = \int \int \int f(x, y) \delta(x \sin \phi - y \cos \phi - s) e^{-i\omega s} dx dy. \quad (111)$$

Due to the sifting property of the Dirac delta function [44], equation (111) can be re-written as:

$$G(\phi, \omega) = \int \int f(x, y) e^{-i\omega(x \sin \phi - y \cos \phi)} dx dy \quad (112)$$

Using the definition of the 2D FT of a function:

$$F(u, v) = \int \int f(x, y) e^{-i(u x + v y)} dx dy, \quad (113)$$

it can be seen from equation (112) that it is just the same as the 2D FT ($F(u, v)$) but u and v are evaluated at:

$$u = \omega \sin \phi, v = -\omega \cos \phi. \quad (114)$$

The steps to compute the projection slice theorem and reconstruct the original data matrix are by taking the RT of the original signal, then computing the 1D Fourier transform of the projection matrix only over the projected coordinates (s). Then the transformed projection matrix is converted to 2D Fourier space by matching the signal output from the 1D FT of the projection (at one angle) to one slice at the same angle of the 2D FT of the original signal:

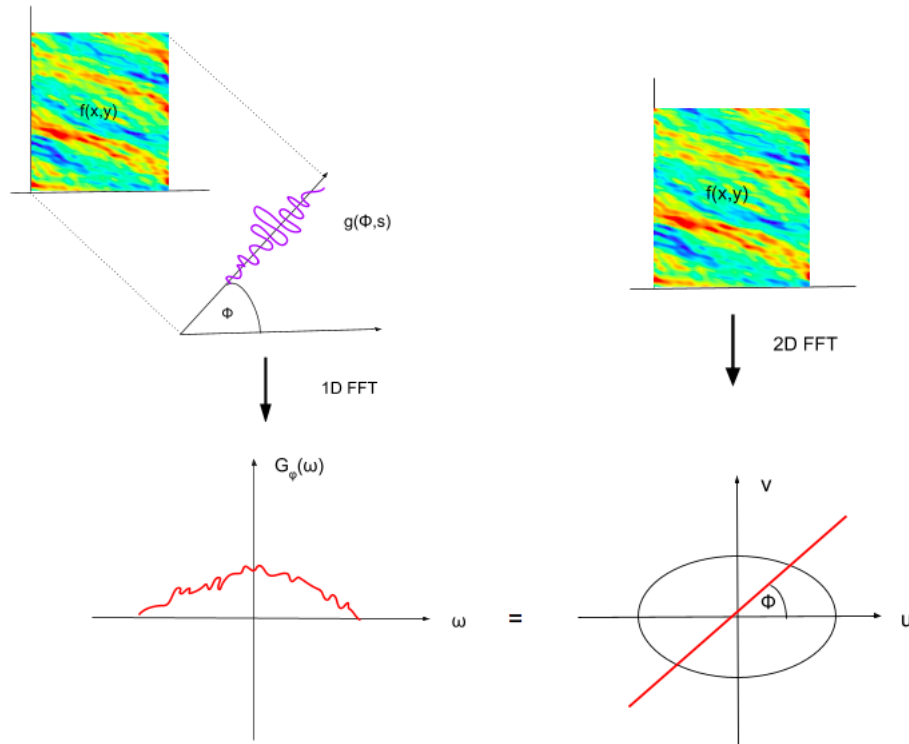


Figure 34: Projection slice theorem.

Figure 34 shows the set up of the projection slice theorem. Focusing on the left half of the diagram, the Hovmoller plot is Radon transformed, then the 1D FT is taken of the Radon transform to create the red, squiggly line (at only one projection angle). Then looking at the right hand side, the original Hovmoller diagram is 2D Fourier transformed. The values on the 2D FT'd line are the same as the one from the 1D FT of that one projection. The original signal is reconstructed when the 1D inverse FT is taken of the 1D FT Radon transform samples.

One important step to keep in mind is that the original signal must be padded with zeros to have the length and width of the image be equivalent to the diagonal of the image. This is to ensure there is minimal loss in resolution and to make sure the image doesn't get cut off when rotating along different angles. For example, when looking at the synthetic sine wave from figure 32a, the figure can be padded with zeros, so each side is equivalent to the size of the diagonal making square dimensions:

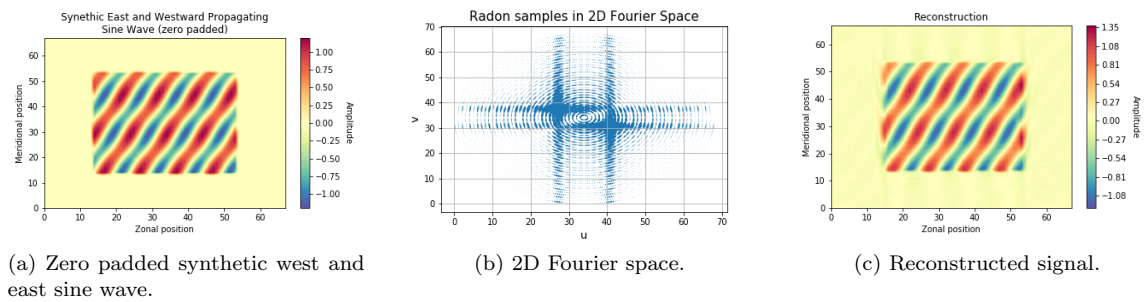


Figure 35: Original signal, transformed, and reconstructed.

Figure 35a shows the zero padded original east and westward propagating sine wave. Figure 35b shows the 1D FT'd Radon transform samples converted from polar into Cartesian coordinates, which is equivalent to 2D FT of the original signal. Figure 35c shows the reconstructed data taking the inverse 1D Fourier transform from the Radon, Fourier transformed data. However, the amplitude of the reconstructed data is a slight overestimation from the original input.

This is due to limitations in reconstruction because the amount of measurements taken for the original function is finite, which leads to the Fourier domain being sampled in a difficult way to work with. Note that the Fourier samples lie in a circular grid rather than square one. Fourier transforms are primarily meant to perform on a square grid, such as the fast Fourier transform [36]. Due to the circular grid format, the sampling distribution is much denser near the origin than the outer regions looking at figure 35b, where there are many more data points near the center.

This implies that there is more data available for lower frequencies, which will result in the lower frequencies to be reconstructed accurately. However higher frequencies, where the more finer details of the original function are located, are not as greatly sampled, which leads to a blurrier reconstructed image. Also the interpolation between the angle resolution, as the angles are in increments of 1° , may result in an inexact reconstructed image. Overall, the reconstructed image is comparable to the original input image, but with the positive amplitude of the reconstructed image being slightly overestimated. The projection slice theorem can be treated as an aside to the relation between the Radon and 2D Fourier transform. The theorem is a way to check that the Radon transform is working properly, which is indicated if the original signal can be reconstructed from it.

References

- [1] Rabitti A., 2016: Understanding the equatorial ocean: theoretical and observational studies. PhD thesis, Utrecht University. 1-190
- [2] Dijkstra H., 2008: *Dynamical Oceanography*. Berlin, Germany: Springer
- [3] Holmes R.M., JN Moum, and LN Thomas, 2016: Evidence for seafloor-intensified mixing by surface-generated equatorial waves. *Geophysical Research Letters*, **43**, 1202-1210
- [4] Gerkema T., H. van Haren, L.R.M Maas, J.T.F Zimmerman, 2008: Geophysical and astrophysical fluid dynamics beyond the traditional approximation. *Reviews of Geophysics*, **46**, 1202-1210
- [5] Gregg M., T. Sanford, D. Winkel, 2003: Reduced mixing from the breaking of internal waves in equatorial waters. *Nature*, **422**, 513-515
- [6] Philander S., 2001: Atlantic Ocean Equatorial Currents. *Encyclopedia of Ocean Sciences*, **2**, 234-237
- [7] Sen Gupta A., A. Ganachaud, S. McGregor, J.N. Brown, L. Muir 2012: Drivers of the projected changes to the Pacific Ocean equatorial circulation. *Geophysical Research Letters*, **39**, 41-47
- [8] Matsuno T., 1966: Quasi-Geostrophic Motions in the Equatorial Area. *Journal of the Meteorological Society of Japan*, **44**, 25-43
- [9] Maas L.R.M., U. Harlander, 2007: Equatorial wave attractors and inertial oscillations. *Journal of Fluid Mechanics*, **570**, 47-67
- [10] Maas L.R.M., 2001: Wave focusing and ensuing mean flow due to symmetry breaking in rotating fluids. *Journal of Fluid Mechanics*, **437**, 13-28
- [11] Gill A., 1982: *Atmosphere-Ocean Dynamics*, Cambridge, MA: Academic Press
- [12] Cushman-Roisin B., J.M. Beckers, 2011, *Introduction to Geophysical Fluid Dynamics*, Cambridge MA: Academic Press
- [13] Holton J., G. Hakin, 2013: *An Introduction to Dynamic Meteorology*, Cambridge MA: Academic Press
- [14] Pinault J., 2018: Resonantly Forced Baroclinic Waves in the Oceans: Subharmonic Modes. *Journal of Marine Science and Engineering*, **78**, 1-25
- [15] Cravatte S., J. Picaut, G.Eldin, 2003: Second and first baroclinic Kelvin modes in the equatorial Pacific at intraseasonal timescales. *Journal of Geophysical Research Atmospheres*, **108**
- [16] Zhu X., A. Kaneko, N. Gohda, H. Inaba, K. Kutsuwada, M. Radenac, 1998: Observation of mixed Rossby-gravity waves in the Western equatorial Pacific. *Journal of Oceanography*, **54**, 133-141
- [17] Weisberg R.H., A. Horigan, C. Colin, 1979: Equatorially trapped Rossby-gravity wave propagation in the Gulf of Guinea. *Journal of Marine Research*, **37**, 67-86
- [18] Pershing A., B. Monger: Coriolis Force Powerpoint Notes. *Cornell University*
- [19] Maas L.R.M., 2016: Wave Attractors, Lecture Notes Utrecht University, 1-167

- [20] Ashkenazy Y., N. Paldor, Y. Zarmi, 2012: A new approximation for the dynamics of topographic Rossby waves. *Tellus A: Dynamic Meteorology and Oceanography*, **64**, 1-14
- [21] Maffei S., A. Jackson, P. Livermore, 2017: Characterization of columnar inertial modes in rapidly rotating spheres and spheroids. *Proceedings of the Royal Society*, **473**, 1-21
- [22] Rushley S., D. Kim, A. Adames, 2019: Changes in the MJO under greenhouse gas-induced warming in CMIP5 models. *Journal of Climate*, **32**, 803-821
- [23] Li T., G. Philander, 1996: On the Annual Cycle of the Eastern Equatorial Pacific. *Journal of Fluid Mechanics*, **9**, 2986-2998
- [24] Ogata T., S. Xie, 2011: Semiannual Cycle in Zonal Wind over the Equatorial Indian Ocean. *Journal of Fluid Mechanics*, **24**, 6471-6485
- [25] Silva I., D. Weis, J. Scoates, J. Barling, 2013: The Ninetyeast Ridge and its Relation to the Kerguelen, Amsterdam and St. Paul Hotspots in the Indian Ocean. *Journal of Petrology*, **54**, 1177-1210
- [26] Prerna s., A. Chatterjee, A. Mukherjee, M. Ravichandran, S. Shenoi, 2019: Wyrтки Jets: Role of intraseasonal forcing. *Journal of Earth System Science*, **128**, 1-18
- [27] Macdonald J., P. Fox, 1990: The Mid-Ocean Ridge. *Scientific American*, **262**, 72-81
- [28] Carlowicz M., S. Schollaert Uz, 2017: El Niño Pacific Wind and Current Changes Bring Warm, Wild Weather. <https://earthobservatory.nasa.gov/features/ElNino>
- [29] Cronin M., M. McPhadden, R. Weisberg, 2000: Wind-Forced Reversing Jets in the Western Equatorial Pacific. *Journal of Physical Oceanography*, **30**, 657-676
- [30] Jochum M., 2006: *Physical Oceanography: Developments Since 1950*. Berlin, Germany: Springer
- [31] Zhang C., 2005: Madden-Julian Oscillation, *Reviews of Geophysics*, **43**, 10-29
- [32] Tang Y., B. Yu, 2007: MJO and its relationship to ENSO, *Journal of Geophysical Research*, **113**, 1-18
- [33] Manz K., The Mid-Atlantic Ridge. <https://whc.unesco.org/en/activities/504>
- [34] Wang L., J. Yu, 2019: Dynamics of Upwelling Annual Cycle in the Equatorial Pacific Ocean. *Sustainability*, **11**, 38-50
- [35] Fruman M., B. Hua, R. Schopp, 2009: Equatorial Zonal Jet Formation through the Barotropic Instability of Low-Frequency Mixed Rossby-Gravity Waves, Equilibration by Inertial Instability, and Transition to Superrotation. *Journal of Atmospheric Science*, **66**, 2600-2619
- [36] Smith S., 1999: *The Scientist and Engineer's Guide to Digital Signal Processing*, San Diego CA: California Technical Publishing
- [37] Sakova I., 2010: Low-frequency modes of variability of the Indian Ocean and their connection with the Indian Ocean Dipole. 65-80
- [38] Chelton D., M. Schlax, 1996: Global Observations of Oceanic Rossby Waves. *Science*, **272**, 234-238

- [39] Cipollini P., D. Cromwell, P. Challenor, S. Raffaglio, 2001: Rossby waves detected in global ocean colour data. *Geophysical Research Letters*, **28**, 323-326
- [40] Cipollini P., G. Quartly, P. Challenor, 2006: Remote sensing of extra-equatorial planetary waves in the oceans. *Manual of Remote Sensing*, **6**, 61-84
- [41] Maharaj, A., P. Cipollini, N. Holbrook, 2009: Multiple westward propagating signals in South Pacific sea level anomalies. *Journal of Geophysical Research Atmospheres*, **114**
- [42] Paldor N., Y. De-Leon, 2019: Commonly used methods fail to detect known propagation speeds of simulated signals from time-longitude (Hovmoller) diagrams. *Ocean Science*, **15**, 1593-1999
- [43] Press W., 2006: Discrete Radon transform has an exact, fast inverse and generalizes to operations other than sums along lines. *Proceedings of the National Academy of Sciences of the United States of America (PNAS)*, **51**, 19249-19254
- [44] Deans S., 1983: *The Radon Transform and Some of Its Applications*, Mineola NY: Dover Publications